SCUOLA DI DOTTORATO
UNIVERSITÀ DEGLI STUDI DI MILANO-BICOCCA

Department of Materials Science

PhD program in Materials Science and Nanotechnology

XXXV Cycle

Topological properties of large-area MOCVD-grown Sb_2Te_3, Bi_2Te_3 and their combination

Locatelli Lorenzo

Registration number 861241

Tutor: Prof. Marco Fanciulli

Supervisor: Dr. Roberto Mantovan

Coordinator: Prof. Marco Bernasconi

ACADEMIC YEAR 2021/2022

Contents

Abstract

Chalcogenide thin films, such as Sb_2Te_3 and Bi_2Te_3, have been under the scientific community's attention since long, due to their application as thermoelectric material. Recently, they are gaining additional interest because of their potential use as Topological Insulators (TIs). TIs are materials that combine the existence of insulating bulk with the presence of surfaces hosting Topological Surface States (TSS). TSS are characterized by a Dirac-like band structure with intrinsic momentum-dependent spin polarization and extremely high mobility. These features translate into the possibility of controlling the magnetization of an adjacent magnetic media by applying an electric field across the TI (charge-to-spin conversion) or vice versa (spin-to-charge conversion), in both cases with very low electrical dissipation and limited operation time. Because of these astonishing electrical properties, they have been proposed as potential materials to boost the integration of spintronic devices into ordinary electronics. However, the main currently used technique to grow TIs is Molecular Beam Epitaxy, which is not suitable to guarantee the TIs' mass production, mainly due to the high cost to be faced when targeting wafers-scaled growth. Achieving the growth of TIs through methods allowing an easier technology transfer is therefore demanding. Among them, chemical methods are thought to be a good solution to achieve conformal TIs' growth on large-area substrates, at a limited cost. In this thesis, I used metal-organic chemical vapor deposition (MOCVD) to optimize the growth of p-type Sb_2Te_3, n-type Bi_2Te_3, and combined Sb_2Te_3/Bi_2Te_3 bilayer, on top of Si(111) intrinsic substrate. The main focus has been to validate the topological behavior of such large-area TIs by a thorough study of their (magneto) electrical and electronic properties. In all cases, the clear existence of TSS has been demonstrated by analyzing the observed weak-antilocalization (WAL) effect and by imaging the band structure with angle-resolved photoemission spectroscopy (ARPES). In all the TIs, there is the existence of a non-negligible contribution to the global transport mechanism arising from the bulk states. This is particularly true in the Bi_2Te_3 single layers, due to the Fermi level crossing the bulk states. A core activity of the thesis's work was therefore dedicated to attempt the Bi_2Te_3's band structure engineering by coupling it with Sb_2Te_3 in a full in-situ MOCVD process. In

particular, with Sb_2Te_3 and Bi_2Te_3 sharing the same crystalline structure, the growth of Bi_2Te_3 on top of Sb_2Te_3 was optimized. By ARPES, we observed a clear shift of the Fermi level towards the Dirac point. As a direct consequence, the bulk contribution to the global transport mechanism is largely suppressed, and this is reflected in the magneto-conductance (MC) shape, which is very close to the cusp-like one expected for ideal TIs where the bulk is insulating. The MOCVD-developed TIs has been finally integrated in simple heterostructures with simple (Co-based) ferromagnetic layers, in order to test their potentiality as spin-charge converters. In particular, by means of spin-pumping ferromagnetic resonance (SP-FMR), the spin-charge conversion occurring in Sb_2Te_3 and the bilayer of Sb_2Te_3/Bi_2Te_3 has been measured by taking advantage of the clear favorable position of the Fermi level close to the Dirac point. For both systems, SP-FMR demonstrated quite a large spin-charge conversion, thus confirming that the MOCVD-grown Si/Sb_2Te_3 and $Si/Sb_2Te_3/Bi_2Te_3$ are promising candidates to be integrated into future spintronic devices based on TIs. The successful growth of the 2D ferromagnet CrTe-based alloy on top of our MOCVD-grown TIs has also been achieved, and the magnetic properties of the 2D ferromagnets were verified by MOKE microscopy, constituting a first step towards the development of a full chalcogenide-based spin-charge converter.

Outline and personal contribution

Within this thesis all the results I collected during my three years long Ph.D activity are summarized. The guideline of the whole work is to demonstrate that by means of metal-organic chemical vapor deposition (MOCVD), it is possible to grow large-area Topological Insulators (TIs) on top of Si(111) substrates, whose functionalities are comparable with those of the TIs grown by physical methods (i.e. molecular beam epitaxy (MBE)). This manuscript is organized in four chapters as it follows. In the first one, an overview of the already existing spintronic devices is reported, with particular care to those based on TIs or relying on spin-orbit torque (SOT) mechanisms and their evolution through the years. In the second chapter are collected all the experimental methods employed within the thesis, highlighting the original procedures that were adopted to interpret some specific data obtained experimentally. Additionally, in chapter two also the structural and morphological characterization of the TIs is reported to keep these well distinguished from the functional results reported in the final chapters. In chapter three the focus are the results obtained on single-layer TIs on Si(111), i.e. without being integrated with ferromagnets (FMs) or other magnetic materials, while in chapter four the attention is moved to the heterostructures composed from a TI and a FM with the aim of studying their possible magnetic interaction and the related spin-charge conversion mechanisms.

The results presented in chapters three and four must be intended as the final scientific outcome of a work that is based on the efforts of many scientists that cooperated to obtain some common results. The next few lines have the aim of guiding the reader through a correct understanding of what is my personal contribution to the thesis. At the beginning of my Ph.D., the group had already succeeded in growing by MOCVD quasi-epitaxial films of Sb_2Te_3 on large-area Si(111), despite such materials had been characterized solely from a structural and morphological point of view. My first task was to perform a thorough magneto-electrical characterization devoted to investigate the topological character of such materials. Subsequently, I had been trained in handling the MOCVD facility with the goal of optimizing the growth of Bi_2Te_3 thin films. I have been involved in the whole optimization process and, once the material reached the epitaxial quality, I focused on its investigation from a functional point of view. The results I obtained on the Sb_2Te_3 film in terms of magnetotransport properties turned out to be crucial for the correct interpretations of the results obtained by means of ferromagnetic resonance (FMR) on stacks composed by Sb_2Te_3/Au/Co/Au. A further activity I carried on regarded the optimization of the chemical-structural and magnetotransport properties of Bi_2Te_3 grown on top of Sb_2Te_3 substrates. The main purpose of this activity was to obtain a band structure engineering of the Bi_2Te_3 top layer by controlling the position of its Fermi level. The successful growth of the Sb_2Te_3/Bi_2Te_3 stack, with the consequent improving of the topological character of the system, motivated me to visit the NCSR 'Demokritos' institute in Greece to perform angle-resolved photoemission spectroscopy (ARPES) on such a sample and to attempt the growth of CrTe-based alloy on top of our MOCVD-grown TIs. Ultimately, the ARPES results moved us towards a first step in the investigation of Sb_2Te_3/Bi_2Te_3/Au/Co/Au hesterostructures by means of FMR-based techniques. The latter activity concluded my scientific research as a Ph.D. student in the context of this thesis.

Chapter 1

Introduction

In 1943, in Pennsylvania at the Moore School of Electrical Engineering, for war purpose, it was assembled what is commonly considered the first electronic computer. Such a machine, called ENIAC, had a dimension of 180 m^2 and a weight of 1000 kg. The power consumption was so high that a black out affected the whole west part of the city during the first time it was switched on. Since than, the technology went through massive advances so that nowadays we are able to build microprocessor with a computing power which is not even comparable with the one of this pioneering machine. Such an impressive advances was possible thanks to the continuous down-scaling of every single components, which is a tremendously topical issue, since it is directly related to the density of electronic component present into a device. In 1965 G. Moore, co-founder of Intel, by evaluating the increasing trend of the amount of electronic component in a single chip made the hypothesis that every year their number doubles. Such hypothesis turned out to be verified with only slight corrections. [1] Currently the miniaturisation challenge mainly relies on the scale down of CMOS transistors which are the building blocks of every electronic device. This scale down process is now approaching limits which are no longer related to technological or manufacturing issues but are intrinsically related to the quantum nature of matter. In order to face such a challenge the scientific community is dedicating huge efforts towards the optimization of electronic components that are based either on different physical principles or on novel materials.

In this context, spintronics, i.e. the branch of electronics that makes use of the electrons' spin as an additional degree of freedom, represents one of the most interesting platform in the view to develop ultra-low power and ultra-fast memory and logic devices. [2]

1.1 Spintronics

In spintronics the electrons' magnetic moment (i.e. the spin) plays a role in determining the transport properties within certain materials. The origin of such a modification of the transport properties is related to the Zeeman energy as defined in 1.1

$$E = \vec{\mu} \cdot \vec{B_{eff}} \tag{1.1}$$

where $\vec{\mu}$ is the magnetic dipole, $\vec{B_{eff}}$ is the effective magnetic field and E is the energy gained from the dipole due to the presence of the field. It is of fundamental importance to consider that $\vec{B_{eff}}$ has to include all the possible origin of magnetic field interacting with the dipole, among which, a permanent magnetization or even complex spin-orbit phenomena that for some particular symmetry of the crystal generate a magnetic field in the reference frame of a conductive electron.

A schematic representation of the typical spin splitting observed in a ferromagnet (FM) is reported in figure 1.1.

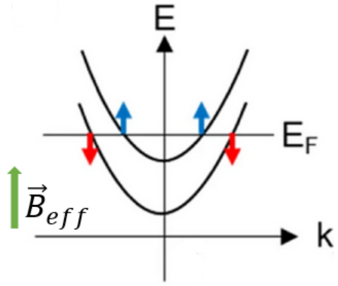

Figure 1.1: Scheme of the spin splitting between upward magnetic moment (blue arrow) downward magnetic moment (red arrow)in an effective magnetic field (green arrow)

In figure 1.1 it can be noticed that around the Fermi level the band structure is spin-dependent and accordingly to the different density of states the amount of spin-up electrons is different from the amount of spin-down electrons.

The difference between the two carriers population gives rise to a global spin polarization which strongly depends on the band structure and could be even engineered by artificially shifting the Fermi level. [3, 4] This phenomenon was addressed as the two-current model and was deeply studied by Albert Fert [5, 6] already within his PhD thesis. In that period were also performed several experiments [5, 6, 7] whose physical interpretation anticipated the results obtained several years later in the late 80's. [8] The experiment consisted in doping a metal (Nickel) with magnetic elements which scattering cross section is strongly spin-dependent. There were employed Cobalt (Co), which mainly interacts with spin-down electrons, and Rhodium (Rh) which strongly scatter just the spin-up electrons. The result was that when Nickel is doped with both Cobalt and Rhodium the resistivity of the materials was massively enhanced while if it was doped with just one of the dopant the resistivity of the material remained constant. The physical mechanism at the basis of such result is that in the case of both the element doping Nickel both the spin population are continuously scattered. On the other hand, if just one of the two elements is employed as a dopant, one of the two channel is left completely open and just one population of electrons is scattered. Such an interpretation paved the way for the realization of a device in which the two dopants, with spin-dependent scattering cross section, were substituted with two ferromagnetic layer. From the study of the two-current model it was known that in a FM any different spin population experience different resistance, depending on the orientation of the magnetization. Thus, by analogy, it was predicted that an heterostructure composed by two ferromagnetic layers separated by a non magnetic (NM) one could show a resistance which strongly depends on the relative orientation of the ferromagnetic layers.

1.1.1 Giant Magnetoresistance (GMR)

The realization of an experiment, aiming to prove this analogy between the ternary alloy (Ni-Co-Rh) and a heterostructure with magnetic pinned and free layers, had to wait almost a decade, due to technical limitation. In 1988 it was then possible to grow a NM layer thin enough to allow spin conservation from one FM to the other, being the typical spin diffusion length of the order of a few nanometers (*nm*). In the mid 80s, with the development of techniques such as MBE, it became possible to fabricate multilayers composed of very thin individual layers, and it was possible to extend the experiments performed on ternary alloys to stack of FM/NM. It was soon demonstrated the mutual analogy between the behaviour of the ternary alloys (Ni-Co-Rh) and the heterostructure, in which a huge difference in the resistance of the structure was observed when the FM layers have parallel or antiparallel magnetization i.e the GMR effect. The experiment was performed with an alternation of Fe (FM) and Cr (NM) layer with the current flowing parallel to the layers, [9] as shown in the scheme reported in 1.2a). The most remarkable result obtained was a GMR of 80% (defined as $(R_{max} - R_{min})/R_{min}$ (where R_{max} and R_{min} represent the resistance of the two states) with a thickness of the Cr equal to 9 nm, at 4.2 K, as shown in 1.2b).

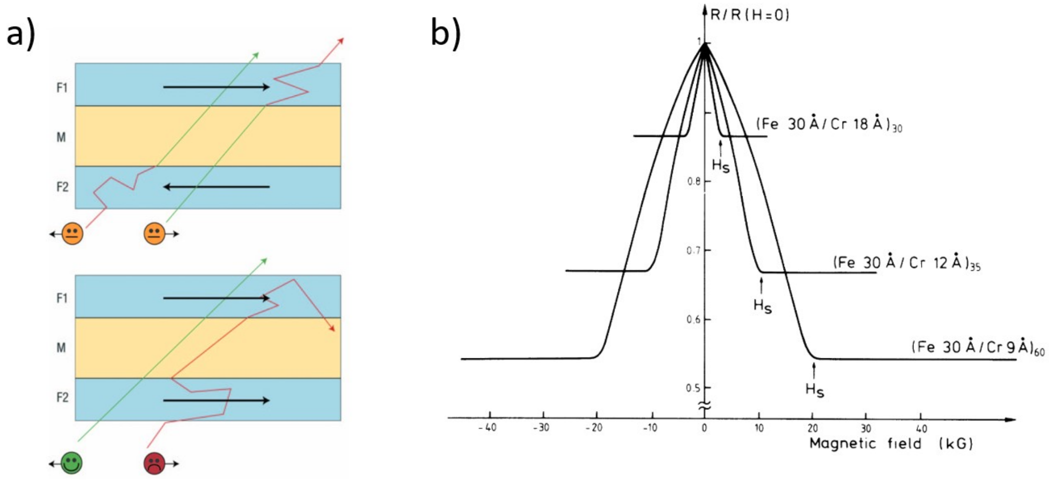

Figure 1.2: Scheme of the current flowing through the multilayer in (a) and the R/R(H=0) signal obtained while changing the magnetization relative orientation of the Fe layers by applying an external magnetic field in (b). Figure adapted from [8, 9].

A classical explanation and a quantum interpretation of the GMR effect were proposed respectively from Camley and Barnas in 1989 [10] and from Levy and Zhang in 1990.[11] The two main phenomena contributing to the observation of the GMR are the reflection across the interfaces, due to strong spin-dependence of the density of states in the FM layer and the spin-dependant scattering probability in the bulk of the FM layers. The two different origins are distinguished by employing different direction of the current flow: one in the plane of the film (CIP) an one perpendicular to the plane of the film (CPP). Technologically the difference in the resistance of a heterostructure when the FMs are parallel or antiparallel could be exploited to encode, in the high or low value of the resistance, the value of a binary bit. Previously to such a discovery, industrial storage devices were based on Hard Drive Disk (HDD) on which a grid of magnetic domains was patterned, by applying a spatially confined magnetic field. The logic value 'O' and '1' were encoded in opposite orientation of the small magnetic domains. The read of the logic values, encoded in the domains' magnetization, was based on the magnetoresistance (MR) measured in the tip while it was passing close enough to the magnetized domains. The read process was clearly the bottleneck of such a technology since the magnetic field, generated by a magnetized domain, has to be enough extended to be sensed by the read-tip, thus limiting the bit density. With the discover of GMR an innovative reading process was proposed employing two ferromagnetic layers, one with pinned magnetization and one with very soft magnetization, thus very susceptible to the magnetization of closer FM. By recording the resistance of the heterostructure it was possible to distinguish between the parallel and antiparallel orientation of the two ferromagnetic layers, thus the logic value of the bit was determined.

The impact of such a discovery was so huge that within 10 years the first GMR-based HDD were commercialized by IBM, tremendously increasing the storage capacity, and later, in 2007 Fert and Grumber deserved the Nobel prize.

1.1.2 Tunnel Magnetoresistance (TMR)

A further development, in line with the original GMR, is the so-called tunnel MR (TMR), which take place when two ferromagnetic layers are separated by a tunnel barrier in the so-called magnetic tunnel junction (MTJ). In a MTJ, the transverse electrical current intensity depends on the relative orientation of the two FMs' magnetization. [12, 13] Typically, in a MTJ one FM has a fixed (i.e. pinned) magnetization direction, while the other has fixed direction but free verse, thus defining two well separated resistance states being low and high when the magnetizations of the FMs are parallel or antiparallel, respectively. The difference between the resistance of these two states normalized to the one with lower resistance, defines the TMR amplitude, which is the MTJ's figure of merit. TMR up to thousands % are nowadays achieved, which heavily contributed to the dramatic jump-up of the storage capacity in HDD. [14]

These two new discovered effects allowed to optimize the energy consumption, the speed and the scalability of the devices used to read the value of the bit, encoded in the magnetization of a ferromagnetic layer, giving rise to the first generation of Magnetic Random Acces Memory (MRAM). At that time the bottleneck of memory devices was represented by the writing part which was done by means of classical magnetic induction which is an extremely energy-consuming and slow operation.
A new MTJ based mechanisms was proposed to overcome the limited performances of such a storage device, with the aim of implementing an alternative writing scheme, suitable for the technological advances in the microelectronics field. [15, 16, 17] It was proposed to design an MTJ composed by a pinned ferromagnetic layer and a free one with the possibility to apply a bipolar current, i.e., from the pinned layer to the free one and viceversa. Starting from an antiparallel configuration, which usually encode the ”0” logic value, with the aim of switching the free layer, electrons are injected from the pinned FM to the free one. The current becomes fully polarized in the first FM thus, the electrons crossing the barrier have a well defined spin, according to the magnetization of the pinned layer. They exert a torque on the magnetization of the free layer, rotating it, to obtain the parallel configuration (”1” encoded). The opposite situation requires the free layer to switch from parallel (”1” encoded) to antiparallel (”0” encoded). This is done by injecting electrons from the free layer to the pinned one. Being the free layer thinner than the pinned one the electrons are not fully polarized, thus the ones aligned to the magnetization of the pinned FM have higher probability to tunnel through the barrier. On the other hands the back-scattering process involves mainly the minority electrons (with magnetic moment antiparallel to the magnetization of both the layers). This results in the accumulation of back-scattered electrons in the free layer. Since these electrons have a magnetic moment

oppositely oriented with respect to the magnetization of the free layer they exert a torque on it, until it is flipped, becoming antiparallel to the magnetization of the pinned layer. Such process is schematically shown in 1.3.

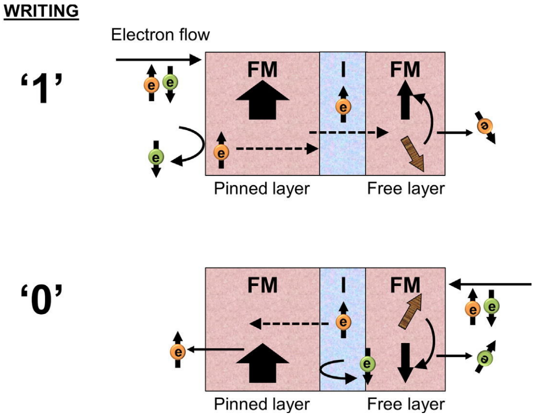

Figure 1.3: Schematic representation of the switching mechanism of the free layer of an MTJ based on Spin Transfer Torque mechanism. Figure adapted from [15]

This technology was firstly implemented by several microelectronics company under the name of Spin Transfer Torque - MRAM (STT-MRAM) [17, 16] with several advantages in speed and power consumption with respect to classical MRAM based on magnetic induction to define the bit value. Despite this, since the current density needed to switch the magnetization of a FM through tunnel effect is quite high, it speed up the detrimental process of the whole heterostructure.

From this point ahead a huge effort has been dedicated from the scientific community to find new ways to electrically manipulate the magnetization of the free layer guaranteeing scalability, higher speed, low power consumption and durability of the device.

“Writing is the problem” is a well-recurring issue along the historical development of MTJs, and several alternative options have been gradually introduced, opening the floor to the development of alternative and most advanced concept than the first MTJ architecture, which are briefly summarized below.

1.1.3 Spin-Orbit Torque (SOT) phenomena

The common thread of these new writing mechanism is related to the employment of Spin Orbit Torque (SOT) effect, which generally identifies a class of phenomena that biunivocally relates a charge current with a spin current i.e Spin to Charge Conversion (SCC) or Charge to Spin Conversion (CSC) phenomena. Several specific mechanisms could be addressed for these aim, such as, Spin Hall effect (SHE), Rashba-Edelstein effect (REE) or Dressellhaus effect (DE) that have a common origin related to the existence of a strong Spin-Orbit Interaction (SOI). Depending on the specific phenomenon considered the driving force of such intense SOI could be the presence of heavy elements Spin Hall Effect (SHE) or the existence of a particular band structure where spin-up and spin-down bands are split. This splitting leads to the generation of a spin-momentum locking i.e., a biunivocal relation between the carriers' momentum and their spin state. All those phenomena, generally classified as SOT effect, have a common characteristic related to the biunivocity of the relation between spin and momentum of the electrons, thus it always exists also the inverse phenomenon.

In figure 1.4 are shown two devices' scheme employing SHE (in panel (a)) and REE (in panel(b))

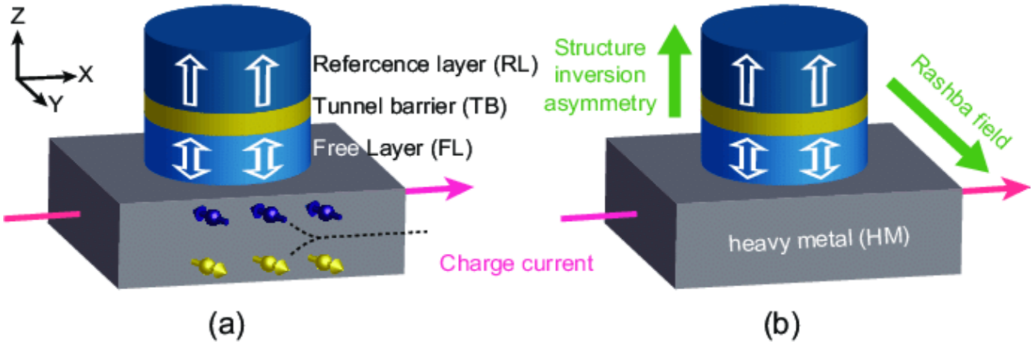

Figure 1.4: SOT-MRAM devices exploiting SHE in (a) and REE in (b). Figure adapted from [18].

The devices shown in figure 1.4 are both identified as SOT-MRAM and they exploit SOT to control the magnetization of the free layer and the TMR effect to read the encoded logic value. With respect to the STT mechanism presented above the advantage of defining the state exploiting SOT is that the current used to encode the ”0” or ”1” state does not flow through the entire device but just through the dedicated ”writing channel”, increasing the durability of the device.

A step further has been recently done by Intel developing a spintronics device suitable for memory application and logic operation, namely the Magnetoelectric Spin-Orbit (MESO) device and a scheme of the device is shown in figure 1.5.

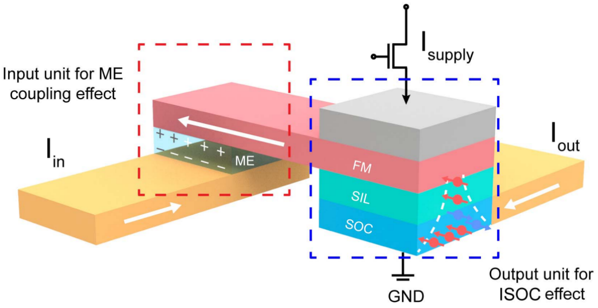

Figure 1.5: Sketch of a MESO memory device. Figure adapted from [19].

The ”writing” exploits a magnetoelectric material that depending on the direction of the current flowing underneath can torque the magnetization of the FM defining its state. On the other hand, the ”reading” is performed by injecting a current in the FM (whose act as a spin-polarizer) which then flows into a material with high Spin-Orbit Coupling (SOC). The spin accumulation in an high SOC material leads to the generation of a transversal charge current whose flow direction depends on the spin polarization of the injected electrons (SCC). In conclusion the MESO device could be seen as a three terminal device in which, when a positive power supply is applied a biunivocal correlation between I_{in} and I_{out} is obtained, thus it constitutes a promising candidate to substitute the CMOS transistor in spin-based logic operations.

During the years the technology evolution in the field of MRAM has attracted huge interest from the scientific community since it represents a possible, promising, alternative to the existing silicon technology. In figure 1.6 it is shown a timeline of spintronic devices from firs MRAM towards the processing-in-memory architecture, with a comparison between the dimension, the operating time and the energy consumption of the devices presented above.

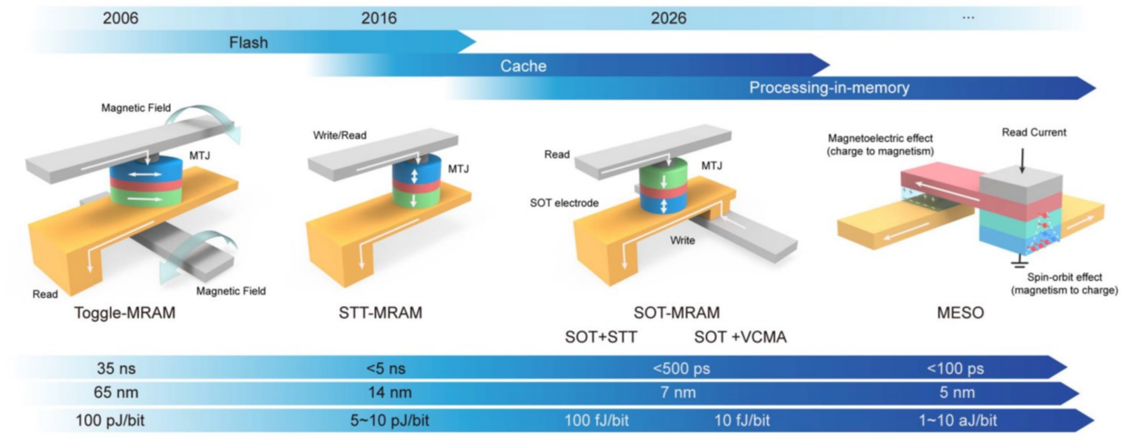

Figure 1.6: Comparison of the energy consumption, dimension and operating time of several device through the years. Figure from ref [20].

It can be noticed how the dimension has been reduced from 60 to 5 *nm*, thus allowing the integration of a huge number of devices in a chip. At the same time also the energy consumption and the switching time have been drastically reduced, thus allowing for the fabrication of chip with high operating speed and huge density of devices. The state of the art of the research is now intensively working to optimize each component of the MESO device to speed-up the writing and the reading process. With this aim, recently, it was proposed to employ a new class of materials, namely the Topological Insulators as high SOC material to push further the efficiency of the 'reading' process.

1.2 Topological matter

Topology is a branch of geometry that studies objects possessing some invariants to a particular class of transformations, such as stretching or deformation. The class of transformation that define a certain topology, indicated with an integer number, (i.e. the Genus) are transformations that operates a continuous deformations, without creating or closing holes. Such transformations are defined as *smooth* transformations and some examples are shown in figure 1.7.

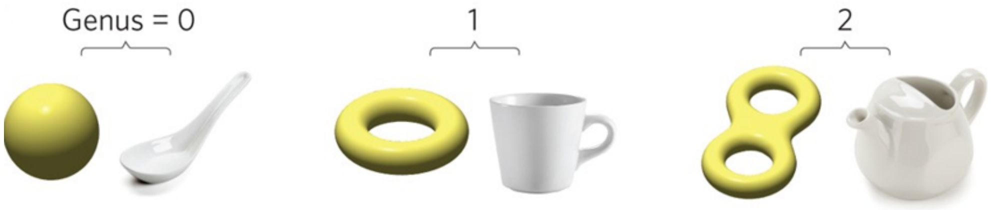

Figure 1.7: Example of some geometries encountering *smooth* transformation that preserves their Genus despite changing their shape

In material science it is well known that the band structure of a material is intimately related to the physical symmetry of the electric potential generated by the crystal. In this context, the band structure of a material can be associated to a topological invariant, i.e. a specified Genus, that is conserved under *smooth* transformations. Topological materials have a well defined genus and at the interface between two materials with a different topology (i.e. Topological material and air or *vacum*), a crossover peculiar state is required to meet and compensate the topology difference.

In the next section it is presented a particular class of topological material which is the main character of the work performed during my thesis.

1.2.1 Topological Insulators (TIs)

A specific class of topological material is composed by three-dimensional Topological Insulators (3D-TI) in which the bulk of the film is insulating while the surface possess delocalized metallic states, characterized by high mobility and spin-momentum locking. The first TI ever synthesized was Bi_xSb_{1-x} in 2008 [21, 22] and subsequently the second generation of TI came as Bi_2Te_3, Sb_2Te_3 and Bi_2Se_3. [23, 24, 25] The surface of such materials shows the typical Dirac-like band structure which is characterized by the existence of linearly dispersed bands around the Fermi energy as shown in figure 1.8.

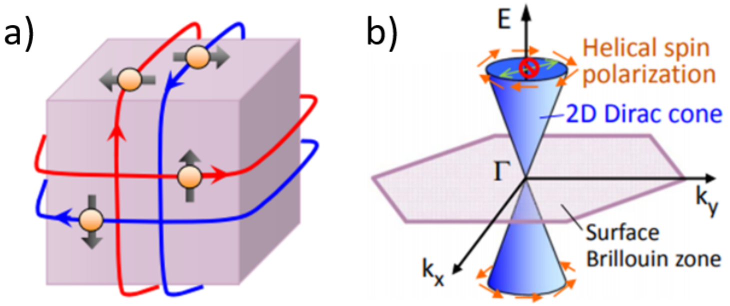

Figure 1.8: Real space representation of the dependency of the spin direction depending on the current direction (a), k-space representation of the Dirac-like, conical, band structure with helical polarization (b). Figure adapted from [26]

In the typical Dirac-like band structure the spin and momentum are locked-up and perpendicular to each others thus, depending on the direction of the injected current, a surface polarization is obtained. Moreover, such electronic states are described by the 2D-Dirac equation which, as known from relativistic quantum mechanics, has as solution the massless Dirac fermions. Observing the conical band structure shown 1.8b) it could be seen that the back-scattering event is forbidden by the helical spin texture. Such a band structure, in a thin film, leads to the generation of two interfaces (one with the air and one with the substrate) that host TSS and a bulk that remains insulating. Thus a current injected into an ideal TI would flow just through the very thin surface of the film, avoiding any bulk dissipation and showing high conductivity and full spin-polarization.

1.3 Spintronics devices and the role of TIs

The high mobility and the spin-momentum locking, typical of TI, have enormous implication in the technological application of these materials in new electronic device. The potential of TI resides in the extremely low power consumption that is required to polarize the current flowing at the edge of the TI and , viceversa, the low power consumption needed to convert a spin current into a charge current, flowing just at the TI's surface. These advantages make such a material extremely promising for the integration in spin logic device such as the MESO from Intel or in any SOT-MRAM device.

In order to quantitatively analyze the effect of the TI on the magnetization state of the adjacent layer it is often considered the current density needed to induce the complete switching of the magnetization of the adjacent FM. This value, obviously, depends on several aspects among which the geometry of the heterostructure, the specific FM employed and its magnetic behaviour. However, the values reported in many reference highlight that in average the current density needed to switch a FM is of the order of $10^5 - 10^6 A/m^2$ exploiting TI [27, 28, 29, 30] and $10^6 - 10^7 A/m^2$ by using ordinary heavy metals (HM). [31, 32, 33]
As an example of the working geometry a picture from [30] is shown in figure 1.9.

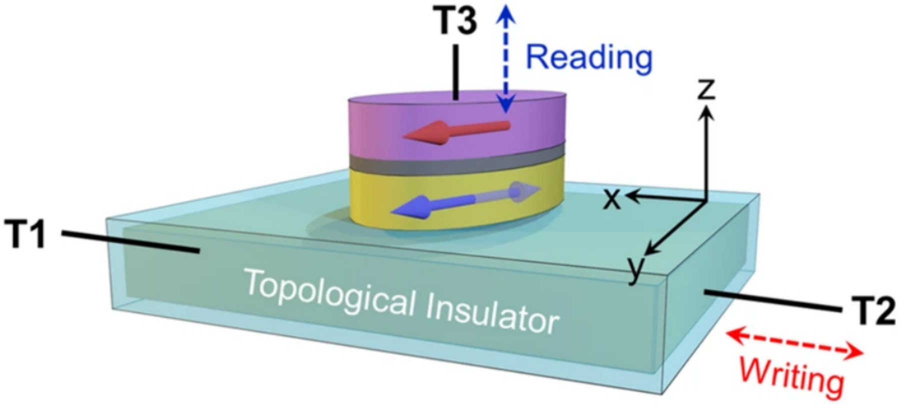

Figure 1.9: Schematic representation of the geometry used in memory devices based on TI to switch the magnetization of a FM. Picture adapted from [30].

The lower current density needed to complete the switching employing TI instead of heavy metal is a key result for technology applications, motivating the research devoted to optimize chemical method for the growth of TI, to accelerate their transfer to the industry market.
To conclude, among the promising technological exploitation of a fully polarized surface it has to be mentioned also to possibility of employing them to control and stablize adjacent magnetic structures as domain walls or skyrmions. Magnetic skyrmions, [34, 35] are topologically protected whirling spin configurations that have been predicted since the end of the 1980s. [36, 37] The main mechanism that gives rise to skyrmions is the competition

between the Dzyaloshinskii-Moriya interactions (DMI) and the exchange interactions. As their spin texture cannot be continuously deformed to obtain another magnetic state (nor ferromagnetic nor antiferromagnetic arrangement of the spin), skyrmions are topologically protected and thus relatively stable structures. Stable magnetic skyrmions nowadays are appealing because of their potential applications in novel spintronic devices, for example, information storage or logic devices based on the controlled motion of these particle-like magnetic nanostructures. Towards this direction it has been suggested [38] that stable skyrmions in materials with high SOC could be controlled by the local spin accumulation generated by the injection of an electric current (CSC). Indeed, being TIs materials with intrinsically high SOC, their potential in controlling and stabilizing skyrmions in adjacent magnetic media is attracting huge efforts from the whole scientific community.

1.4 Overview on TIs growth methods

The need for these sharp and smooth surface required the researchers to tackle the growth of TIs by means of MBE, which is an atomically controlled, physical deposition technique. Since MBE allows to obtain high quality films with extremely sharp surface and controlled stoichiometry, it represented a perfect work platform to investigate the TSS in single layered TI and SOT phenomena in TI-FM heterostructure. [39, 40] Despite the high potential of MBE in material science it could be difficult to employ it in mass production due to its very high cost when the growth of several inches samples are needed

With the aim of boosting the integration of TI into ordinary electronics it is of certain interest to study the possibility of synthesizing them employing chemical methods. Despite chemical growth methods are usually considered less precise than the physical counterparts, recently highly controlled Atomic Layer Deposition (ALD) and Metal Organic Chemical Vapor Deposition (MOCVD) growths have been demonstrated to produce high quality TIs, sometimes with a nearly epitaxial order. [41, 42] The main difference between chemical growth methods and physical ones is related to the fact that physical processes rely on the evaporation and subsequent condensation (physical transformation) of the elements involved in the growth, while chemical processes rely on the chemical reactions that are induced between the reactive elements. Due to this different nature a clear advantage of Chemical Vapour Deposition (CVD) is related to the uniformity of the growth on large scale, that could be achieved even on substrates containing 3D step-like microstructures.

Chapter 2

Experimental methods

2.1 Metal Organic Chemical Vapour Deposition (MOCVD) of TIs

The general working principle of an ordinary CVD process is based on the introduction of the reactants in the growth chamber, in the required proportions, at a selected temperature and partial pressure. In the specific case of MOCVD the reactants are obtained by means of sublimation or evaporation of metal-organic compounds called 'precursors', that incorporate the reactant elements. In the case of liquid precursors they are contained within bubblers, kept at a precise temperature and pressure to control the amount of reactant elements that are delivered to the growth chamber. The amount of reactant which is transported to the reactor is ultimately controlled by selecting the flow of the inert gas (usually H_2 of N_2) from the bubblers to the reactor. Considering all the parameters that influence the materials' flow from the bubblers to the reactor it could be stated the following relation:

$$\nu = \left(\frac{P_v f_v}{KT_{std}}\right) \cdot \frac{P_{std}}{P_{cyl}} \tag{2.1}$$

where ν is the molar flow in mol/min, P_v is the vapour pressure of the MO precursor at the bath temperature, f_v is the volume flow rate of the carrier gas in l/min, K is the gas constant, T_{std} and P_{std} are the room temperature and the atmospheric pressure respectively, and P_{cyl} is the total pressure of the employed bubblers.

Practically, the carrier gas is forced to flow through the bubblers, where, due to the controlled pressure and temperature, the amount of reactant in gas phase is fixed. The combination of the bubblers' temperature, internal pressure, and gas mass flow set the concentration and amount of precursor that volatilizes into the reactor. By employing the above described method the molar flow of each precursor is settled with a precision of the order of μmol/min. After the precursors in vapour phase are injected into the growth chamber a supersaturation condition is obtained, i.e. the system is brought out of thermodynamic equilibrium. To restore the equilibrium condition the reactants start to deposit on the substrate, thus, lowering the concentration of the species in the gas phase and realising the 'vapour to solid' transition.

A picture of the MOCVD present at the CNR-IMM unit of Agrate Brianza is shown in 2.1.

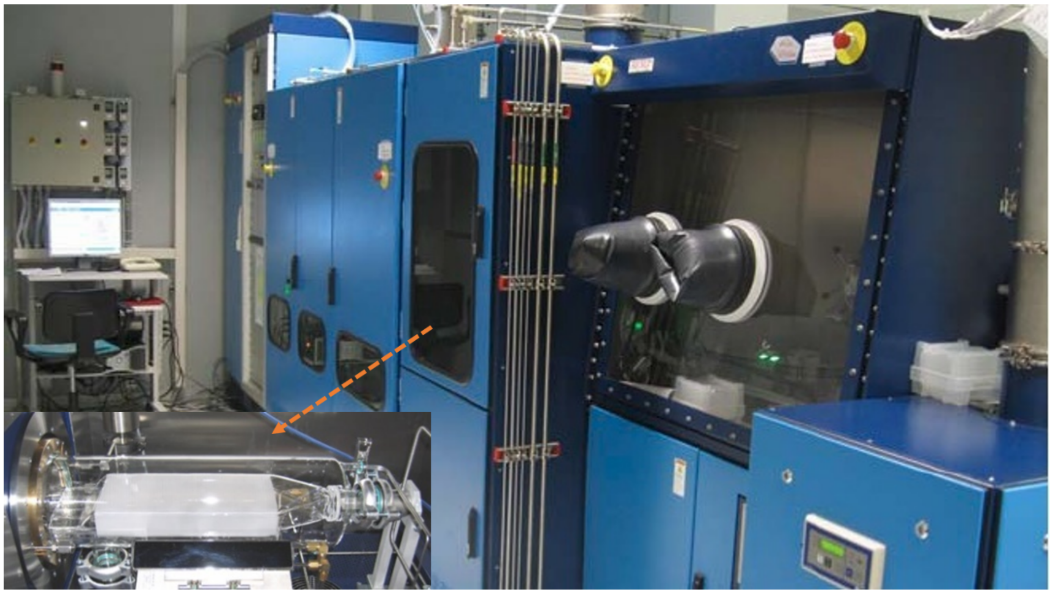

Figure 2.1: MOCVD system installed at the CNR-IMM laboratory at Agrate Brianza. The inset shows a zoom on the chemical reactor with the space for a 4" wafer.

If a proper tuning of the parameters is performed and epitaxial quality is achieved, the process is defined Metal Organic Vapour Phase Epitaxy (MOVPE). An epitaxial layer obtained by means of MOVPE is a fundamental achievement for material science and industrial application considering that, nowadays, the most spread growth technique used to obtain epitaxial layers is MBE. As a matter of fact, MOCVD is already widely employed at industrial level, for instance in the Nitrides production for LED applications. [43] It is therefore, of high interest the attempt of employing the MOCVD technology also for spintronics applications, exploiting emerging materials such as topological insulators. This is one of the reason that motivated the recent efforts at the CNR-IMM Unit of Agrate Brianza to develop MOCVD processes to synthesize epitaxial-quality Sb_2Te_3 and Bi_2Te_3 thin films on Si-based substrates. [41, 42]

The growth where performed by employing Aixtron AIX 200/4 MOCVD tool equipped with an IR-heated 4” rotating graphite susceptor. Electronic grade precursors were loaded into bubblers thermalized at 20.0 (±0.1) °C and delivered to the reactor chamber through the vapor-saturated ultra-pure N_2 carrier gas.

Antimony Telluride (Sb_2Te_3) and Bismuth Telluride (Bi_2Te_3) grown by MBE have reached high epitaxial quality [44, 45] and the existence of TSS and insulating bulk was demonstrated by means of magnetotransport measurement and angle resolved photoemission spectroscopy (ARPES). [23, 25, 46, 47] It is of primary importance for the integration of MOCVD-grown TI in industrial electronics to optimize the growth of high quality Sb_2Te_3 and Bi_2Te_3 on top of large-area Silicon substrate. Both Sb_2Te_3 and Bi_2Te_3 films, were optimised in a lengthy process during which, starting with some reasonable chemical assumptions, the growth process was attempted a large number of times by slowly varying one parameter each time. In the next sections a brief explanation of the selected parameters employed to grow the TIs by MOCVD will be reported.

2.1.1 MOCVD of Sb_2Te_3

Prior to the deposition of Sb_2Te_3, the Si(111) substrates were treated to remove the native oxide layer with HF (10% in deionized H_2O) for 3 min, thoroughly rinsed with deionized H_2O, and N_2-dried. Subsequently, the samples were quickly loaded into the glove box, in a controlled atmosphere poor of O_2 (less than 12 ppm). The first growth step consists in a pre-growth thermal treatment, needed to remove all the residual Oxygen molecule and to ensure the substrate surface is smooth and free from other contaminants. The pre-growth annealing was performed *in-situ* at 500 °C for 60 min at 20 mbar, with total N_2 flow of

11000 l min^{-1}. After, the reactor temperature was brought back at 25 °C the growth process can start.

The precursors employed were antimony chloride ($SbCl_3$) and bis(trimethylsilyl)telluride ($Te(SiMe_3)_2$). The depositions is carried out at 25 °C for 90 min at 15 mbar, with a total flow of 5.575 l min^{-1}, and setting the precursors vapor pressures at 2.28 and $3.32 \cdot 10^{-4}$ mbar for $SbCl_3$ and $Te(SiMe_3)_2$, respectively. After the deposition an *in-situ* post-growth annealing was performed with the aim of improving the out-of-plane and the in-plane relative orientation of the crystals' grain. The post-growth annealing procedure consists in a first heating ramp performed at 900 mbar and 5.575 l min^{-1} N_2 flow, with temperature passing from 25 °C to 300 °C. The second step consists in a 15 min annealing performed at constant pressure and N_2 flow (900 mbar and 5.575 l min^{-1} respectively). Subsequently, a three-step cooling ramp is performed at 990 mbar and 1.5 l min^{-1} N_2 flow: from 300 °C to 200 °C in 20 min, from 200 °C to 100 °C in 35 min and then from 100 °C to 50 °C in 20 min.

By means of X-Ray inspection and various microscopical techniques the crystalline structure was properly characterized (see section 2.5). Employing X-Ray reflectivity (XRR) the thickness was found to be 30 nm (20 nm/hour) with a Route Mean Square (RMS) roughness of $\approx$ 1nm. The X-Ray diffraction(XRD) pattern was collected in the Bragg-Brentano geometry and the rhombohedral crystalline structure was revealed and the Full Width at Half Maximum (FWHM) of the [006] peak was measured along the rocking angle axis. In this experimental configuration, the evaluation of the FWHM provides information about the mosaicity of the crystal, which quantifies the broadening of the out-of-plane orientation of the crystalline grains of the film. For rhombohedral crystals such as Sb_2Te_3, a lower mosaicity implies a better alignment of the c-axis (out-of-plane) of the crystals lattice. The reported values is 0.46°, which is interpreted as the signature of a quasi-epitaxial film where the crystalline grains are extremely aligned out-of-plane. Transmission Electron Microscopy (TEM) and Scanning Electron Microscopy (SEM) were carried out confirming the 30 nm thickens and the quasi-epitaxial hexagonal structure, through the Fast Fourier Transform (FFT). The optimization of the Sb_2Te_3 film, from a structural point of view, passed through the analysis of films grown on the substrate without any pre-treatment (as-deposited), following the annealing of the substrate (pre-annealed) and combining the substrate annealing with a post growth annealing (post-annealed). The detailed structural and morphological investigation of: as-deposited, pre-annealed and post-annealed films is thoroughly reported in [41] with clear evidence of the better quality of the post-annealed film. During the optimization of the MOCVD process to grow Sb_2Te_3, it was fundamental to characterize the magneto-transport properties of the layers towards the investigation of their topological properties. This was an important part of my work during the first year of Ph.D. and the results are summarized in [48].

2.1.2 MOCVD of Bi_2Te_3

In the case of Bismuth Telluride (Bi_2Te_3) the growth process is performed at high temperature, thus it does not require thermal treatments, not prior nor after the growth. Electronic grade trimethylbismuth ($BiMe_3$) and disopropyltellurium (DiPTe) were employed as Bi and Te precursors, respectively. The growth is performed at 350 °C, 75 mbar and the duration is set at 180 min with a total flow of 4.5 l mim^{-1} setting the precursor's vapor pressures at $4.20 \cdot 10^{-3}$ and $7.80 \cdot 10^{-3}$ mbar for $BiMe_3$ and DiPTe, respectively. [42]
Similarly to what was done with Sb_2Te_3 the films were characterized from a crystallographic point of view by means of X-Ray and microscopy technique (see section 2.5). The thickness of Bi_2Te_3 was determined observing a TEM cross section image and it results equal to 90 nm. The crystalline structure is explored by means of XRD technique and the rhombohedral arrangement is evident and then confirmed by the FFT performed on the TEM image. The mosaicity is derived as reported in 2.1.1 and is equal, in Bi_2Te_3, to 0.26°, thus, the crystal grains are even more aligned out-of-plane than in the case of Sb_2Te_3. As expected, this implies a smoother surface, as verified with the AFM from which is derived a RMS value equal to 0.5 nm. The detailed description of the growth optimization process and the structural characterization are reported in [42].

2.1.3 MOCVD of Sb_2Te_3/Bi_2Te_3

Antimony telluride and bismuth telluride have the same crystal symmetry belonging to the space group $R\bar{3}m$ and slight different in-plane lattice constant (a) being 0.42 nm and 0.44 nm for Sb_2Te_3 and Bi_2Te_3 respectively. Therefore, in principle they could grow favourably one on top of the other. Historically, the motivation to create such a heterostructures comes from the fact that Bi_2Te_3 and Sb_2Te_3 have different carriers, electrons (n) and holes (p), respectively, and their vertical stacking could therefore naturally realize a topological p-n junction. In such heterostructure the bottom layer could influence the position of the Fermi level of the top one, as recently proposed by growing Bi_2Te_3-Sb_2Te_3 heterostructures by MBE . [49, 50] In this context, as suggested from the band structure that will be discussed in section 3.1.5, we deposited Bi_2Te_3 on top of Sb_2Te_3 with the aim of minimizing the BS-related conduction in the TI by shifting the Fermi level towards the Dirac point (see section 3.1.5).

The growth is performed starting from the growth of the first layer of Sb_2Te_3 , the cleaning procedure and the annealing of the substrate are done exactly as described for Sb_2Te_3 (see section 2.1.1). The material's layer is then grown, keeping unchanged the parameters previously selected to obtain the optimal growth of the single layer of Sb_2Te_3, and the $in-situ$ post annealing is performed after the growth. Without opening the reactor the layer of Bi_2Te_3 is then grown on top of Sb_2Te_3, keeping the parameters employed to grow single-layer Bi_2Te_3 unchanged.

The bilayer is then characterized by means of AFM and X-Ray diffraction to investigate its morphological and structural properties (see section 2.5). The AFM measurement show a roughness expressed in RMS of ~ 3 nm which is slightly higher than both single layer Sb_2Te_3 and Bi_2Te_3. This result is probably due to the fact that Bi_2Te_3 in this context is not grown on perfectly smooth and flat Si(111) but rather on Sb_2Te_3 that, despite being quite flat (RMS ~ 1 nm), it introduces its own roughness in the stack.

The heterostructure is then characterized from a crystallographic point of view by means of XRD and the rhombohedral arrangement is revealed. Due to the thickness of the top Bi_2Te_3 layer of 90 nm such value is completely associated to the top film.

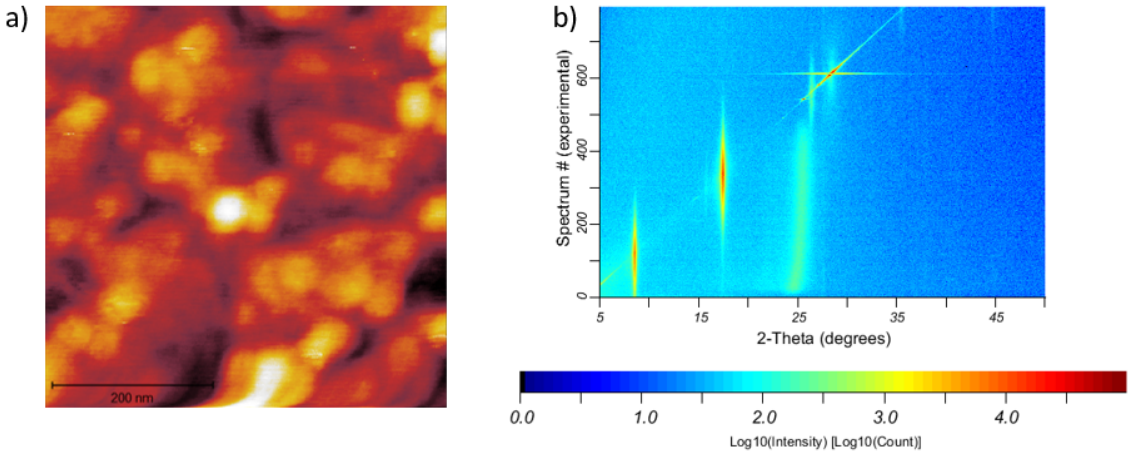

Figure 2.2: In (a) the AFM measurement performed on a square of 0.5 μm^2 . In (b) the Bragg-Brentano XRD map highlighting the 00l peaks of Bi_2Te_3 .

2.2 Magneto-electrical characterization

The electrical characterization was performed in the Van der Pauw configuration on $\sim$ 1x1 cm^2 samples in the 5-295 K temperature range, without any prior processing or capping of the film. The latter measurements were conducted at a constant applied current as provided by a Keitlhey 2610, with the voltage recorded by a Keitlhey 2182A nanovoltmeter. External magnetic field up to 0.8 T was applied at a variable direction with respect to the samples' plane to obtained the desired information.

The conduction parameters of interest are the resistivity (ρ), the mobility (μ) and the carrier density (d(n, p)). The resistivity is obtained by averaging the resistance measured along the four edges of the squared sample, while varying the direction of the current. (Van der Pauw method [51]) The application of an external magnetic field is employed to generate the transversal Hall voltage which is recorded to derive the conduction parameters. Depending on the positive or negative slope of the Hall voltage as a function of the magnetic field it is possible to identify weather the carriers are holes (p) or electrons (n). The carrier density and the mobility can be derived by using equation 2.2 and 2.3.

$$d(n,p) = \frac{IB}{teV_H} \tag{2.2}$$

$$\mu = \frac{1}{ed(n,p)R_s} \tag{2.3}$$

Where V_H is the Hall voltage, e is the electron charge ($e = 1.6 \cdot 10^{-19} C$), t is the thickness of the film, R_s the sheet resistance which is equal to ρ divided by the thickness of the film and B indicates the magnitude of the applied magnetic field.

The mean free path (MFP) can be derived, by employing equation 2.4 as obtained from the semiclassical Drude model:

$$MFP = \frac{\mu k_F \hbar}{q} \tag{2.4}$$

Where k_F is the Fermi wave vector, $\hbar$ is the reduced Plank constant and q is the charge. The estimation of the k_F could be performed by looking to the ARPES spectra and will be detailed in section 3.1.5. Considering that the ARPES spectra are taken at RT, in order to derive the MFP in the 5 – 290 K temperature range, we assume constant k_F as a function of the temperature, with only the bands occupation state varying.

2.3 Investigation of the topological character in the TIs

From an electronic point of view the signature of the TSS resides in some particular features of the magnetoconductance (MC). In disordered electronic systems at room temperature the electronic motion is diffusive, thus, it is assumed that between two points an electron can encounter a certain number of scattering events. Classically, in a many-electrons system, the resistivity experienced by an electron is directly proportional to the number of collision that occurs between two points but, if the temperature decrease enough, quantum interference effect have to be included in the model. In this fashion, when the electron-electron quantum interaction is considered, the most likely path of a single electron is found to be slightly bent as if it belonged to a loop. In materials with strong SOC the two possible rotation directions are associated to a different spin orientation thus, they encounter destructive interference, which results in a global electronic delocalization, defined as Weak anti-localization (WAL). The quantum delocalization of the electrons produces an increment of the global conductivity which holds until the clockwise and the counterclockwise loop are equally probable. The application of a perpendicular magnetic field clearly makes one of the two loops more likely than the other, thus the delocalization effect does not hold anymore and the global conductivity quickly decreases. A sketch of the destructive interference that originates the WAL is shown in figure 2.3a) while in figure 2.3b) it is shown the fast decrease of the MC which take place in the small magnetic field regime due to the break of the time reversal symmetry.

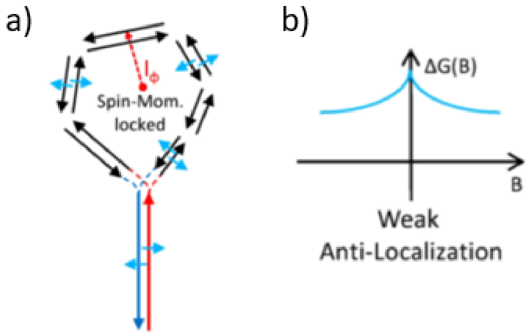

Figure 2.3: Schematic illustration of the destructive interference between time reversal paths in (a) and the behavior of the conductance in a small magnetic field in (b). Figure adapted from [52].

2.3.1 Weak anti-localization (WAL) effect and Hikami-Larkin-Nagaoka (HLN) analysis

The quick decrease of the conductivity as a function of the applied magnetic field is the signature of the WAL effect which is a proof of the existence of a strong SOC in a delocalized many-electrons system. Such an effect was deeply investigated by Hikami, Larkin and Nagaoka in 1980 [53] and an equation describing the phenomena was derived as HLN equation (see 2.5).

$$\Delta\sigma(B) = -\alpha\frac{e^2}{\pi h}\left(\Psi\left(\frac{1}{2}+\frac{h}{8\pi e l_\phi^2 B}\right) - ln\left(\frac{h}{8\pi e l_\phi^2 B}\right)\right) \tag{2.5}$$

In Equation 2.5 Ψ represents the digamma function, h is the Plank constant, e is the electron charge, B is the perpendicularly applied magnetic field and α and l_ϕ are the HLN parameters. In this model α is connected to the number of conductive channels in which the transport mechanism is driven by quantum diffusion and the coherence length (l_ϕ) represents the average distance along which the spin phase is conserved. Within the HLN model, a negative α value is associated to the presence of WAL, with α = - 0.5 in the hypothesis that WAL originates from the TSS belonging to one of the two TI surfaces, or α = - 1 if both TSS contribute to the electronic transport. [54] Values of α different from the previous ones indicate a mixed situation, where the transport across the TSS is not ideal due to the intermixing between the BS and TSS. In the case of non-ideal TI the quantum effect is superimposed to the classical decrease of the conductivity as a function of the perpendicular magnetic field due to the ordinary MR effect. Several phenomena contribute to the classical MR its influence on the MC is often approximated by means of a Taylor expansion in the magnetic field truncated at the second order ($C \cdot B^2$). [55]

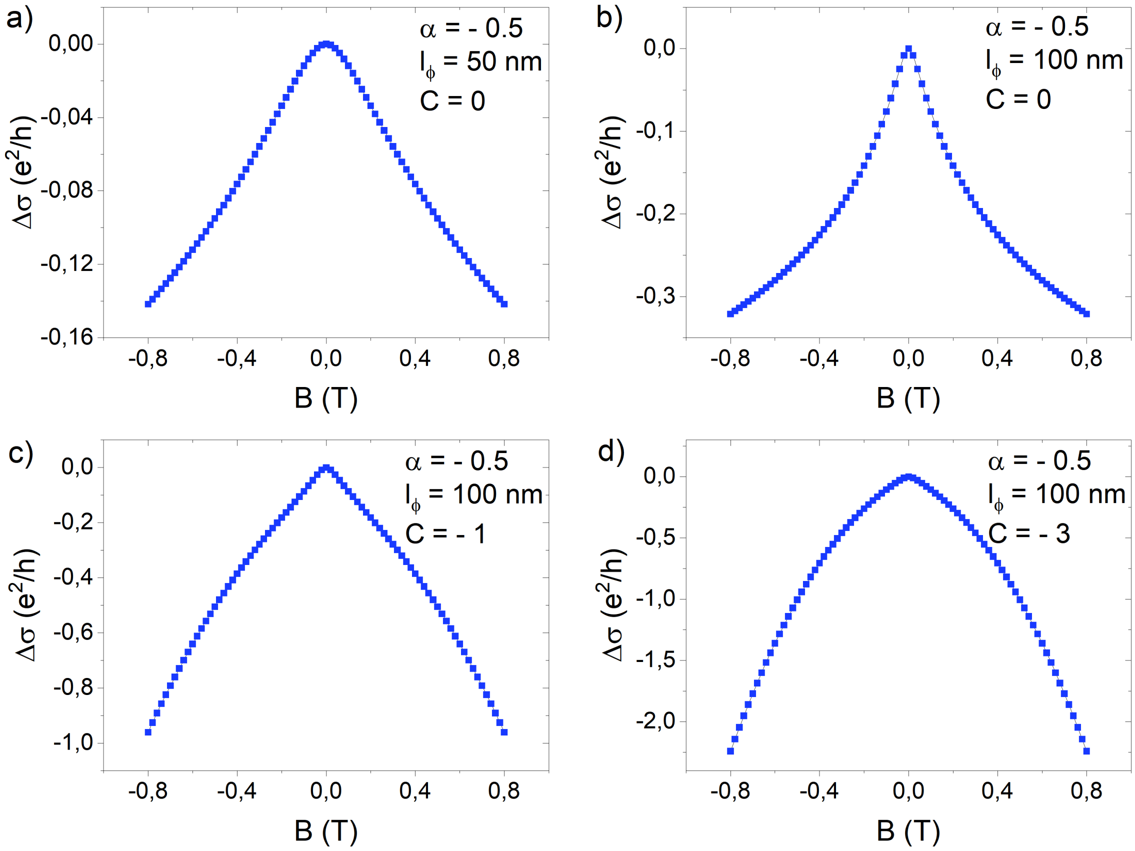

Figure 2.4: $\Delta\sigma$ obtained from 2.6 by employing several meaningful combination of α, l_ϕ and C. Between panels a and b just the coherence length varies being 50 nm in a and 100 nm in b. Both panels show signals that are not affected by classical contribution. In panels c and d the classical parabolic contribution is added with a different amplitude encoded in the C parameters which is -1 in c and -3 in d

The four examples of computed $\Delta\sigma$ displayed in figure 2.4, show how the different combination of the parameters α, l_ϕ and C influences the shape of the $\Delta\sigma$. Of particular importance is the fact that an increase in the coherence length produces an extremely cusp-like signal as evinced from the comparison of 2.4a) and 2.4b). In the panels c and d of 2.4 it is added, with different magnitude, a parabolic signal to simulate the contribution of ordinary BS to the magneto-electrical transport. It is evinced that despite both the $\Delta\sigma$ in 2.4(c,d) contain a relevant contribution from the TSS ($\alpha = -0.5$, $l_\phi = 100nm$) the cusp-like shape is partially hidden in (c) and almost not visible in panel (d). Following these considerations, to properly investigate any acquired $\Delta\sigma$, the correct approach would be to add the parabolic term to the HLN equation as shown in equation 2.6.

$$\Delta\sigma(B) = -\alpha\frac{e^2}{\pi h}\left(\Psi\left(\frac{1}{2}+\frac{h}{8\pi e l_\phi^2 B}\right) - ln\left(\frac{h}{8\pi e l_\phi^2 B}\right)\right) + C\cdot B^2 \qquad (2.6)$$

2.3.2 Angular dependence in WAL

Being the WAL effect directly related to the existence of many-electrons which are delocalized and experience a high SOC, such an effect is not necessarily due to the existence of TSS at the surface of a TI and/or its interface with the substrate. For example, in conductive bulk materials, where the presence of HM give rise to an intense SOC, WAL could be observed as well. [56] To distinguish between the TSS originated WAL and BS-originated WAL it is often adopted a method based on symmetry considerations. To reveal whether the WAL is TSS (2-D) originated BS (3-D) originated it was proposed a method based on the application of an external magnetic field at various angles with respect to the plane of the sample. In this configuration, if the WAL effect is generated by 2-D conduction channels, due to geometrical considerations, the WAL observed must be proportional solely to the perpendicular component of the applied magnetic field. [57]

In our investigation, we conducted angular dependent studies to investigate the role of TSS (or at least, 2D-type of conduction) in determining the observed WAL signals, see sections 3.4. The obtained results, jointly with direct imaging, as provided by ARPES, constitute a clear proof of the existence of TSS in the MOCVD-developed TIs.

2.3.3 Angle Resolved Photoemission Spectroscopy (ARPES)

The most direct signature of the existence of TSS in TIs is the presence of a connection between the bulk valence band and the bulk conduction band. Such a connection is formed by linearly dispersed bands that intersect each other in the so-called Dirac point (DP). Such an energy dispersion relation represents the solution of the relativistic Dirac equation, it shows spin-momentum locking and the particles belonging to these states behave as massless fermions. To image the TSS, it is employed the Angle Resolved Photoemission Spectroscopy (ARPES) technique, which requires that the surface of the TI is free from oxide and as smooth as possible. This requirement does not represent an issue whenever the TSS imaging is performed $in-situ$ straight after the growth, however, since we performed the ARPES measurement $ex-situ$ a delicate procedure is required to prepare the surface.

The treatment of the surface is performed in two stages: a sputtering, used to remove the Oxygen and Carbon atoms from the surface, and an annealing, needed to recover and smoothing the surface. The sputtering is performed employing Ar^{+} ion at 1.5 KeV and a pressure of 10^5 for an arbitrary duration. To verify that the Oxygen and Carbon atoms have been correctly removed from the surface a chemical inspection is performed by means of X-Ray Photoemission Spectroscopy (XPS) (see section 2.5). On the other hands, the smoothness of the surface after the annealing is probed by means of Reflection High Energy Electron Diffraction (RHEED) (see section 2.5). The physical parameters and the duration of the sputtering and the annealing process are discussed later in section 3.1.5 being different for the different films investigated.

ARPES is a technique based on the tracking of the momentum and the energy of electrons ejected from a material after the exposure to a flux of incoming photons with the proper kinetic energy. It is possible to define the energy as a function of the momentum of the ejected electrons in the K-space, thus the image of the band structure ,below the Fermi energy, could be reconstructed. A fundamental characteristic of ARPES is that, being the penetration depth of the employed photons limited the first few material's layer, it is extremely sensitive to the surface band structure. Several typical band structure observed in

TI are shown in figure 2.5.

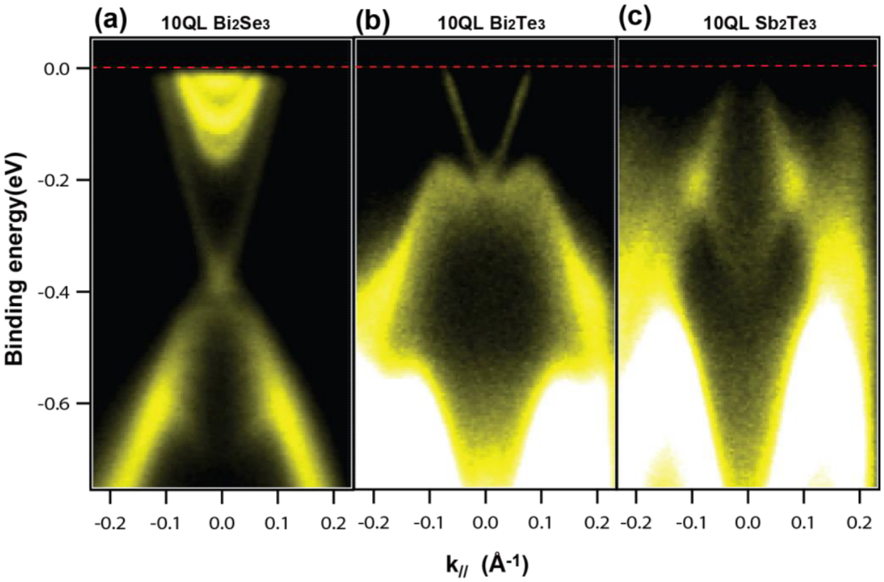

Figure 2.5: ARPES example from the supplementary information of [58]. In the three figures it is clearly visible the connection between valence and conduction states and the different position of the Fermi level influences the states that participate to the electrical transport.

The three panels in Figure 2.5 show the band structure of different TI evidencing that the TSS are clear and well defined in all the three materials. The main difference between the band structures of the three TI is the position of the Fermi level. In the case of Bi_2Se_3 (2.5a)) the Fermi level is deeply in the bulk conduction band, in Bi_2Te_3 (2.5b)) it crosses the TSS without touching the conduction states but far from the Dirac point and in Sb_2Te_3 (2.5c)) it cut the TSS very close to the DP.

The combination of ARPES with the WAL investigation (2.3) is of fundamental importance to precisely localize the topological states in the film. By means of the angular dependent WAL analysis it was possible to confirm that the WAL signal originates from the 2D-TS and not from 3D-BS due to the presence of heavy elements (see 2.3.2. However, from the MC analysis it is not possible to understand if the topological states are located exactly at the films' surface or at one of the Van der Waals planes located between two quintuple layers of the film at a random position within the bulk.

The ARPES employed is part of a complex MBE system present at the Demokritos institute in Athens (see figure 2.6), the system is composed by a main MBE growth chamber and several instrument (XPS, ARPES and RHEED) that can be employed while keeping the sample in ultra-high *vacum* (10^{-10} mbar).

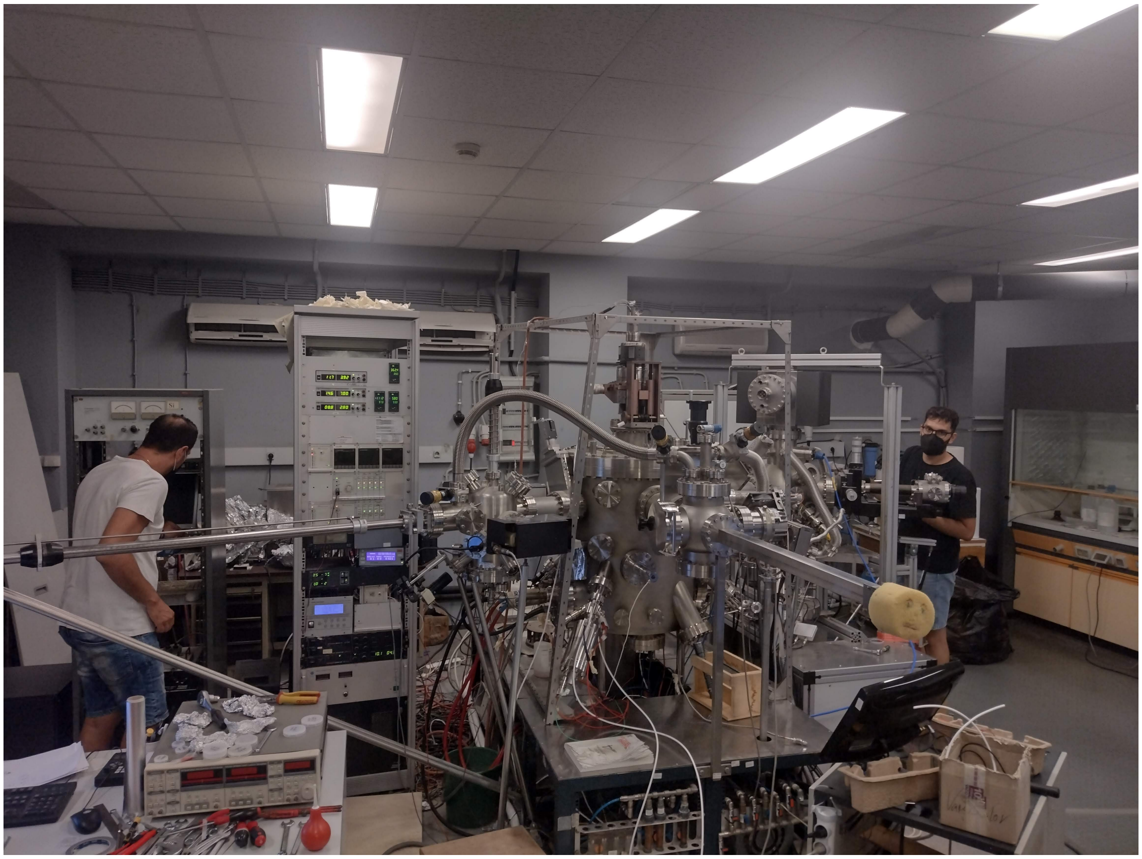

Figure 2.6: Picture of the MBE system in the Demokritos institute in Athens. The various tubes are employed to transfer the film from the main MBE chamber to all the other instrument (XPS, ARPES, RHEED) while keeping it under ultra-high *vacum*.

2.4 Spin-charge conversion in TI/FM heterostructures

The study of the interfacial spin transport and the SCC mechanisms taking place at the interface of FM/TI and FM/heavy metal (HM) systems plays a fundamental role for the future application of spintronic devices. The latter phenomena can be investigated through different experimental techniques, such as SOT [59, 32, 60], spin Seebek effect [61], spin pumping (SP)[62, 63],etc., all based on the conversion between spin and charge currents (see section 1.1.3). This conversion may take place in the bulk or either in the surface states of a material, thus arising from the so-called Spin Hall Effect (SHE)/Inverse Spin Hall Effect (ISHE) [64], or from the Edelstein Effect (EE)/Inverse Edelstein Effect (IEE), respectively. [65] The SHE/ISHE arises from strong spin-dependent scattering processes due to the presence of the SOC interaction, which is particularly relevant in heavy materials (e.g. Pt, Pd, Ta, etc.). As a result of the SHE/ISHE, the electrons flowing in a SOC material separate according to their spin, generating a spin accumulation of opposite signs at the boundaries of the material. The figure of merit to estimate the efficiency of the SCC in a SHE/ISHE based mechanism is the dimensionless quantity called spin-Hall angle (θ_{SHE})/Inverse Spin Hall Angle (θ_{ISHE}). Differently, the SCC in the EE and IEE is not originated in the bulk states, being completely confined in the NM surface states. Here, the relevant quantity to evaluate the SCC and CSC efficiency is the EE/IEE length q_{EE}/λ_{IEE}, which is measured in *nm* .

In section 4.1, the SCC efficiency will be evaluated through SP measurements, thus the ISHE and IEE are the figures of merit to evaluate the SCC efficiency in the presented FM/TI systems.

As introduced in Section 1.3, the surface states of TIs are characterized by intrinsic spin-momentum locking, thus they could be employed to push the SCC efficiency by decreasing the power dissipation with respect to HM, where the SCC take place in the whole bulk. However, being TIs usually composed of heavy elements when coupled with a FM the SCC could derive both from ISHE (bulk effect) and from IEE (TSS-originated) and their disentanglement is not straightforward. Such a difficulty is also evident by reviewing the literature where, for example, two different groups working on a similar CoFeB/Bi_2Se_3 systems provided two different interpretations of the observed SCC, interpreting the observed results both in terms of ISHE [66] and of IEE.[67]

2.4.1 Spin-pumping by FMR (SP-FMR)

A spin pumping experiment can be conducted by means of ferromagnetic resonance (FMR) spectroscopy namely SP-FMR. [62, 63] Here, the precessional motion of the magnetization in the FM generates a pure spin current which is subsequently injected in the NM layer and here converted in a charge current. In the SP theory, such a spin current is related to an enhancement of the damping constant $\Delta\alpha$, which influences the dynamic of the magnetization vector ($d\vec{M}/dt$) in a ferromagnetic material and is described by the Landau-Lifshitz-Gilbert equation with an extra damping term:

$$\frac{d\vec{M}}{dt} = -\mu_0\gamma\vec{M}\times\vec{H}_{eff} + \frac{\alpha_{ref}}{M_s}(\vec{M}\times\frac{d\vec{M}}{dt}) + \frac{\Delta\alpha}{M_s}(\vec{M}\times\frac{d\vec{M}}{dt}) \tag{2.7}$$

Where μ_0 is the vacuum magnetic permeability, γ is the electronic gyromagnetic ratio, $\vec{H}_{eff}$ is the applied magnetic field M_s, the saturation magnetization. Being the cross product between two vectors always perpendicular to them, the first term of the right side of equation 2.7 represents the precessional motion of $\vec{M}$ around $\vec{H}_{eff}$. The second term describes the spiraling of the FM film, being α_{ref} the damping constant of the free-standing FM layer, when not influenced by the presence of an adjacent NM layer. Ultimately, the third therm, is formally equal to the second, with the difference that $\Delta\alpha$ represents the extra-damping introduced into the dynamic equation to justify the generation of the extra spin current due to a spin sink (i.e. NM). The total damping is finally written as:

$$\alpha_{tot} = \alpha_{ref} + \Delta\alpha \tag{2.8}$$

and according to Ref. [68] can be related to the transmission of the spin current across the FM/NM interface. Thus, equation 2.8 can be expressed as

$$\alpha_{tot} = \alpha_{ref} + Re(g_{eff}^{\uparrow\downarrow})\frac{g\mu_B}{4\pi M_s}\frac{1}{t_{FM}} \tag{2.9}$$

where t_{FM} is the thickness of the FM layer and $Re(g_{eff}^{\uparrow\downarrow})$ is the real part of the so-called spin mixing conductance, which quantify the amount of spin-current crossing the FM-spin-sink interface. Within equation 2.7 the unknown magnetic parameters are: γ, M_s, α_{ref} and $\Delta\alpha$ and all of them can be calculated as detailed below. As described in [69, 70], γ and M_s are derived by fitting the resonance frequency as a function of the resonant magnetic field, i.e. $f_{res}(H_{res})$ with the Kittel equation (see equation 2.10)

$$f_{res}(H_{res}) = \frac{\gamma}{2\pi}\sqrt{H_{res}(H_{res}+4\pi M_{eff})} \tag{2.10}$$

where for FM thin films can be considered $M_{eff} \sim M_s$. On the other hand, α_{tot} in a FM is obtained by fitting the signal linewidth at FWHM, $\Delta H^{FWHM}(f_{res})$, obtained in a typical FMR experiment with equation

$$\Delta H^{FWHM}(f_{res}) = \frac{4\pi\alpha}{\gamma} f_{res} + \Delta H_0 \tag{2.11}$$

where ΔH_0 is the inhomogeneous broadening and the obtained α describes the damping in the whole stack investigated by FMR.

The expression for the 3D spin current (J_S^{3D}) generated in the FM layer as a consequence of the extra damping term in Equation 2.9 was calculated in ref. [68] and could be expressed as:

$$J_S^{3D} = \frac{\hbar}{4\pi} \frac{Re(g_{eff}^{\uparrow\downarrow})}{M_s^2} \vec{M} \times \frac{d\vec{M}}{dt} \left(\frac{2e}{\hbar}\right) \tag{2.12}$$

where λ_s is the spin diffusion length in the SOC material. It has to be pointed out that if $t_{NM} << \lambda_s$, the spin current will be reflected at the interface between the SOC material and vacuum, thus lowering the net spin current crossing interface. To integrate in equation 2.12 the back-flowing current, the net spin current results

$$J_{S,net}^{3D} = J_S^{3D} \left(1 - e^{\frac{-2t_{NM}}{\lambda_s}}\right) \tag{2.13}$$

Finally by solving the LLG equation (Eq. 2.12), J_S^{3D} at the equilibrium condition (when $\vec{M}$ and $\vec{H}$ are aligned) the J_S^{3D} can be expressed as:

$$J_S^{3D} = \frac{Re(g_{eff}^{\uparrow\downarrow})\gamma^2\hbar h_{RF}^2}{8\pi\alpha^2} \left(\frac{\mu_0 M_s \gamma + \sqrt{(\mu_0 M_s \gamma)^2 + 4\omega^2}}{(4\pi M_s \gamma)^2 + 4\omega^2}\right) \left(\frac{2e}{\hbar}\right) \tag{2.14}$$

Equation 2.14 represents the general description of the magnetization dynamics when a spin current is considered in the magnetization dynamics. As a result of the SCC, a 3D or 2D charge current can be generated in the NM layer if the ISHE or IEE are considered, respectively. Th current (I_c) is experimentally measured by means of a nanovoltmeter connected to the edges of the FM/NM stack, and it is employed to calculate the following figures of merit to extract the SCC efficiency of the system:

$$\theta_{ISHE} = \frac{I_c}{W J_S^{3D} \lambda_s tanh(\frac{t_N}{2\lambda_s})} \tag{2.15}$$

in the case of ISHE, and

$$\lambda_{IEE} = \frac{I_c}{W J_s^{3D}} \tag{2.16}$$

for the IEE. For a detailed description of the SP-FMR experimental procedure please refer to [71].

2.5 Other methods

In this section a resume of all the experimental techniques employed within the thesis is reported. These methods are usually employed to do the standard characterization of the MOCVD-grown TIs, prior to their functional characterization.

2.5.1 Atomic Force Microscopy (AFM)

AFM was employed to characterize all the samples fabricated during the thesis, from a morphological point of view. AFM is performed by scanning the surface of the film under inspection by means of an extremely sharp tip that is kept at a constant distance from the atoms composing the film's surface thank to atomic forces. An extremely fast and precise feedback loop is responsible to move the tip up and down while the tip is scanning the surface of the material in order to keep the atomic force constant. By recording the movement of the tip it is then possible to reconstruct a map of the morphology of the surface. By evaluating the map over a desired area it is possible to extract the average roughness of the surface, which usually is expressed in Rout Mean Square (RMS) by squaring each height value in the dataset, then taking the square root of the mean.

2.5.2 X-Ray

X-Rays are employed to characterize from a structural point of view each film that was measured electrically during the thesis. X-rays measurements are performed by means of a HRXRD IS2000 four circle goniometer equipped with a Cu K_α radiation (λ = 1.5406$\AA$) and a curved 120° position sensitive detector (Inel CPS-120). During all the measurements the X-ray tube is maintained at 40 kV and crossed by a current of 9 mA. By employing this instrument several characterization could be performed and of particular interest for this thesis i can mention the X-ray Reflectivity (XRR), the X-Ray Diffraction (XRD),the XRD in the Bragg-Brentano geometry (BBXRD) and the φ-scan XRD (φ-XRD). The combination of these techniques allows for a complete characterization of the films from a structural point of view providing the thickness (XRR) the out-of-plane and in plane crystals arrangement (XRD and φ-XRD) and the distribution of the crystals' axis composing the film to evaluate the overall quality of the material (BBXRD).

2.5.3 X-Ray Photoemission Spectroscopy (XPS)

XPS is a spectroscopy technique in which soft X-rays (1-1.5 eV) are used to excite bound electrons through the photoelectric effect and measure their electron binding energy. A necessary condition to perform XPS is that the energy of the incident photons ($h\nu$) is higher than the binding energy of the material's electrons, i.e. the work function ϕ. The binding energy is indeed obtained by means of the folowing relation:

$$E_B = h\nu - E_K - \phi \tag{2.17}$$

Where E_B is the photoelectron binding energy and E_K is the measured kinetic energy of the emitted photoelectron. By employing photon with energies in the soft X-ray spectrum it is possible to excite bonding electron which energy could span from few tens of eV below the Fermi level to a thousand of eV below it. Soft x-rays have a small penetration length within the material ($\sim 10\,nm$) and due to the probability of the photoemitted electron to be reabsorbed in the materials usually the chemical composition deduced from the analysis is attributed to the first 5-7 nm of material. [72] It is of fundamental importance, to notice that with XPS, beside identifying the element present at the film's surface it is possible to reveal the various bounds between the different species identified. As an example, in the case of Sb_2Te_3, it would be possible to distinguish between the energies of Sb-Te and Sb-O or Te-O to verify the exidation state of the surface. Moreover, by comparing the amount of electron detected at each energy is possible to determine the relative amount of each kind of bound on the film's surface.

2.5.4 Reflection High Energy Electron Diffraction (RHEED)

RHEED exploits an electron gun to strike electrons on the surface of a material with a very low angle with respect to the surface and following their diffraction from the surface atoms due to constructive and disruptive interference a particular pattern is detected on the detector. A scheme of a RHEED system is shown in Figure 2.7.

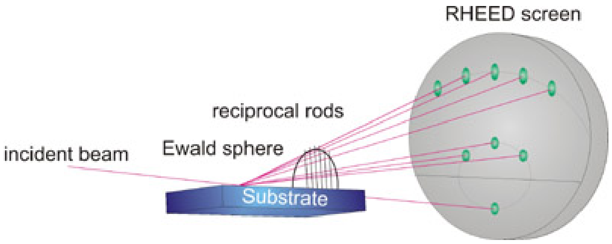

Figure 2.7: Working scheme of a general RHEED system

The electrons energy is usually between 10 KeV and 100 KeV. Such energies would leads to a large penetration depth, however due to the fact that the incidence angle is settled between 1° and 5° just the first few nanometers of materials are responsible for the scattering of the electrons. By employing a kinematic approach in which just elastic scattering are considered it can be written down the condition for constructive interference between electrons scattered from different nucleus, also known as Laue condition:

$$\vec{R}(\vec{k}-\vec{k'}) = 2\pi n \tag{2.18}$$

Where $\vec{R}$ is the vector pointing from one scattering center to the other, $\vec{k}$ and $\vec{k'}$ represents the wave vector of the incident and scattered electron, respectively and n is an integer number. This condition results in the creation of discrete scattering spot on the RHEED screen were the Laue condition is satisfied It is then clear that a necessary condition to observe constructive and disruptive interference on the RHEED screen is clearly the existence of an ordered lattice, thus amorphous material or damaged crystals would generate an interference pattern.

2.5.5 Magneto-Optical Kerr Effect (MOKE) microscopy

MOKE microscopy is a characterization technique widely spread in the material science field that take advantage of the change of polarization to which light is subjected after the reflection from a magnetized surface. MOKE microscopy is based on contrast between two opposite directions of the magnetization and, in our case, it is employed to distinguish between upward or downward magnetization direction in a perpendicular magnetic anisotropy film. Combining a MOKE microscopy with a properly controlled magnet it is possible to track the effect of the magnetic field on the magnetization of a sample. Moreover, in the case the maximum magnetic field applicable is higher than the coercive field of the material investigated it is possible to observe a full switch of the magnetization with the MOKE microscopy.

Chapter 3

Validation of the topological character in MOCVD-grown TIs

Within this chapter are detailed all the results obtained, so far, about the investigation of the topological properties of the MOCVD-growth Sb_2Te_3 and Bi_2Te_3 as single layers and in the form of heterostructure, composed by both layers. The TIs' single layers have been thoroughly characterized, both magneto-electrically and from an electronic point of view, by band structure imaging. We report here also the first experiments conducted on $Si/Sb_2Te_3/Bi_2Te_3$ that allowed us to obtain very promising results, paving the way for a deeper investigation of the properties of these TI-heterostructure.

3.1 Sb_2Te_3 and Bi_2Te_3

3.1.1 Electrical characterization of TIs

The resistivity, extracted as explained in section 2.2, of the MOCVD-grown Sb_2Te_3 and Bi_2Te_3 thin films are shown in figure 3.1 (a) and (b), respectively, in the 5 - 290 K temperature range.

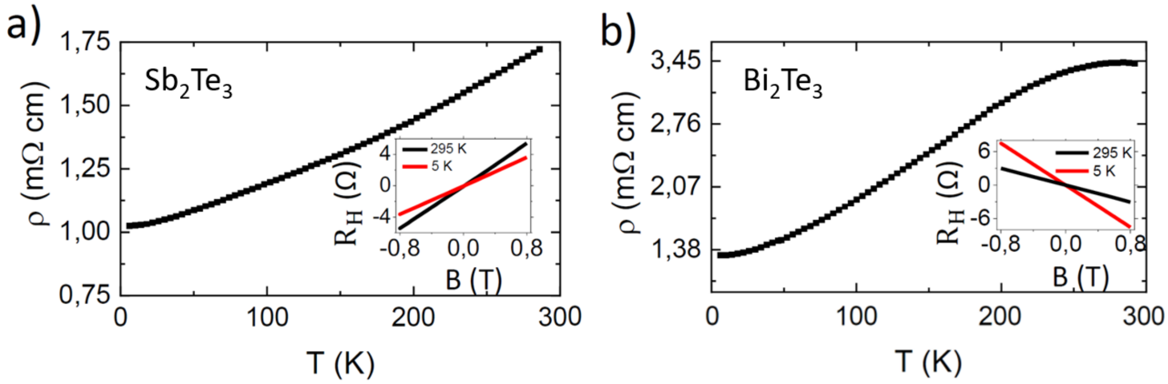

Figure 3.1: Conduction parameters for Sb_2Te_3 and Bi_2Te_3 in panel (a) and (b) respectively.

As can be observed in figure 3.1, both the films, when cooled down from 295 K to 5 K, show a metallic behaviour with an observed 40% and 60% overall resistivity decrease, for Sb_2Te_3 and Bi_2Te_3 layers, respectively. This is in accordance with [44, 73, 74, 75, 76] and such a behaviour indicates that the conduction from BS plays a relevant role in the electronic transport mechanism, differently from the theoretical prediction for ideal TIs. [25, 77] Nevertheless, the fabrication of thin films where the bulk conduction is totally suppressed requires an extreme precision in the engineering of the Fermi level position, which constitutes a remarkable challenge. The main technical issue concerns the typical narrowness of the chalcogenide-based TIs band and the unintentional doping provided by the presence of defects or by slight stoichiometric variations. [23, 78] Due to these reasons, in absence of a fine band structure engineering, TIs often show a metallic character dominated by the BS. [54, 57, 79, 80] The character of the carriers is extracted from the slope of the Hall-voltage (see insets in figure 3.1) and, as expected, it is found to be p-type and n-type respectively in Sb_2Te_3 and Bi_2Te_3. [54, 44, 74] The carrier density ($d(n,p)$) and the mobility (μ) were also extracted from the Hall resistance as described by equation 2.2 and 2.3 and the obtained values are reported in figure 3.2 (left scale).

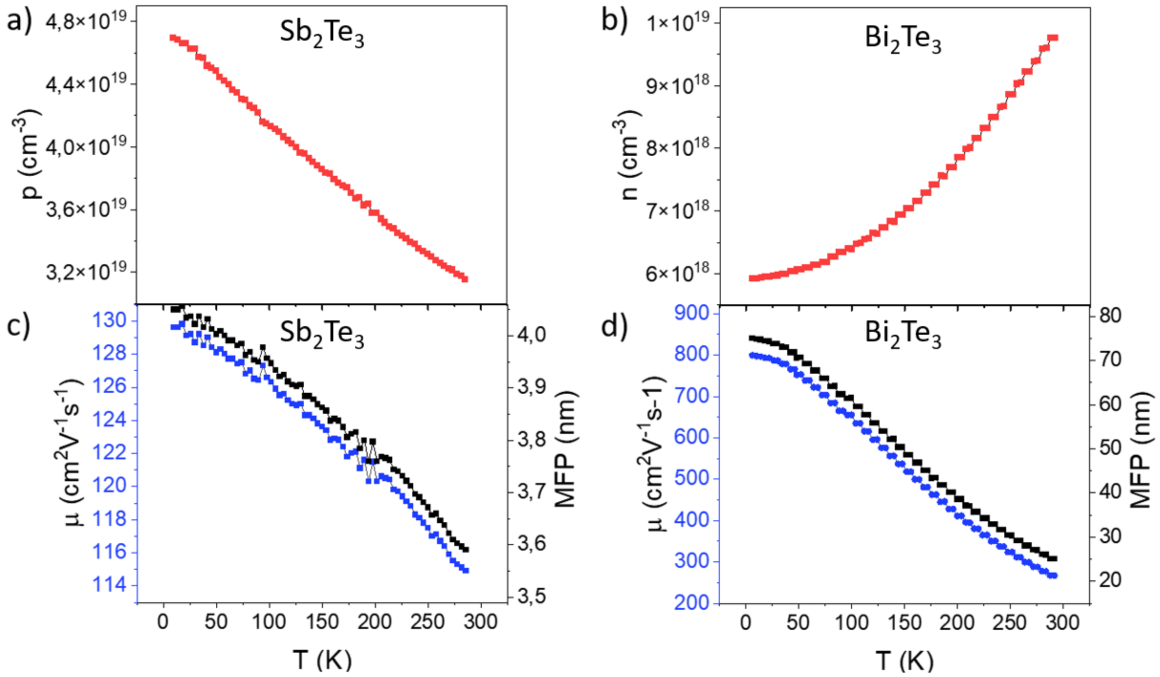

Figure 3.2: Hole density in panel (a) and electron density in panel (b) for Sb_2Te_3 and Bi_2Te_3 respectively. Panel (c) displays the mobility (in blue) and the mean free path (in black) for Sb_2Te_3, while in panel (d) the mobility (in blue) and the mean free path (in black) for Bi_2Te_3 are shown. Figure adapted from the SI of [81].

In figure 3.2 also the Mean Free Paths (MFPs) are reported (right scale of the panels (c) and (d), black line). The MFPs are calculated employing equation 2.4 as derived from the Drude model, following an approximation discussed in section 2.2. As explained in section 2.2 the k_F for both the material are deduced from the ARPES spectra (see section 3.1.5) and the results are: $k_F \sim 0.05 \AA^{-1}$ for Sb_2Te_3 and $k_F \sim 0.15 \AA^{-1}$ for Bi_2Te_3. The MFPs, in the Drude model, are interpreted as the average distance an electron travels before an elastic scattering events occurs. On the other hands, the l_ϕ, as presented in section 2.3.1, represents the average spin conservation distance, thus the l_ϕ and the MFP of the same films have to be compared to understand how many elastic scattering usually occurs before a spin flip event. Indeed, as it will be thoroughly discussed in section 3.1.2, the ratio l_ϕ/MFP strongly influences the shape of the MC measured. Such a ratio, is also particularly meaningful to properly interpret the γ parameter, as defined in equation 3.1, which quantifies the relative contribution of the TSS in the global conduction mechanism and will be discussed in section 3.1.2.

3.1.2 Weak anti-localization analysis and HLN fit

The shape of the MC, representing the conductivity expressed as a function of the applied magnetic field, encodes several information about the material under investigation. As explained in section 2.3 the MC can be analyzed in the framework of the HLN model to investigate the TSS features and their commitment in the electronic transport mechanism of a TI. The applied magnetic field swaps from -0.8 T to +0.8 T with steps of 0.02 T and the MC is recorded from room temperature (RT) to $\sim 5K$. For simplicity it is defined the quantity: $\Delta\sigma$, as the MC signal referred to zero magnetic field and expressed in unit of e^2/h.

As thoroughly described in [81], the equation 2.6 can be employed to fit $\Delta\sigma$, thus extracting the HLN parameters α and l_ϕ, jointly with the quantity C that quantifies the BS contribution. In order to highlight the pure WAL effect, once C is extracted from equation 2.6, the quantity $\Delta\sigma - C \cdot B^2$ can be obtained, which is analyzed with equation 2.6. Such an "iterative" process is very useful for both displaying a clearer WAL effect (see figure 3.3), and to further validate the HLN model by comparing the α and l_ϕ obtained in the two cases (C=0 and C$\neq$ 0).

The next sections summarize the results obtained in the single layers Sb_2Te_3 and Bi_2Te_3 (section 3.1.2) and the results obtained for Sb_2Te_3/Bi_2Te_3 heterostructure (see section 3.2.1). Figure 3.3 displays $\Delta\sigma$ as a function of the, perpendicularly applied, magnetic field for Sb_2Te_3 (a,c) and Bi_2Te_3 (b,d). The data shown are "as measured" in (a,b) and without the B^2 contribution in (c,d), as explained in section 2.3.

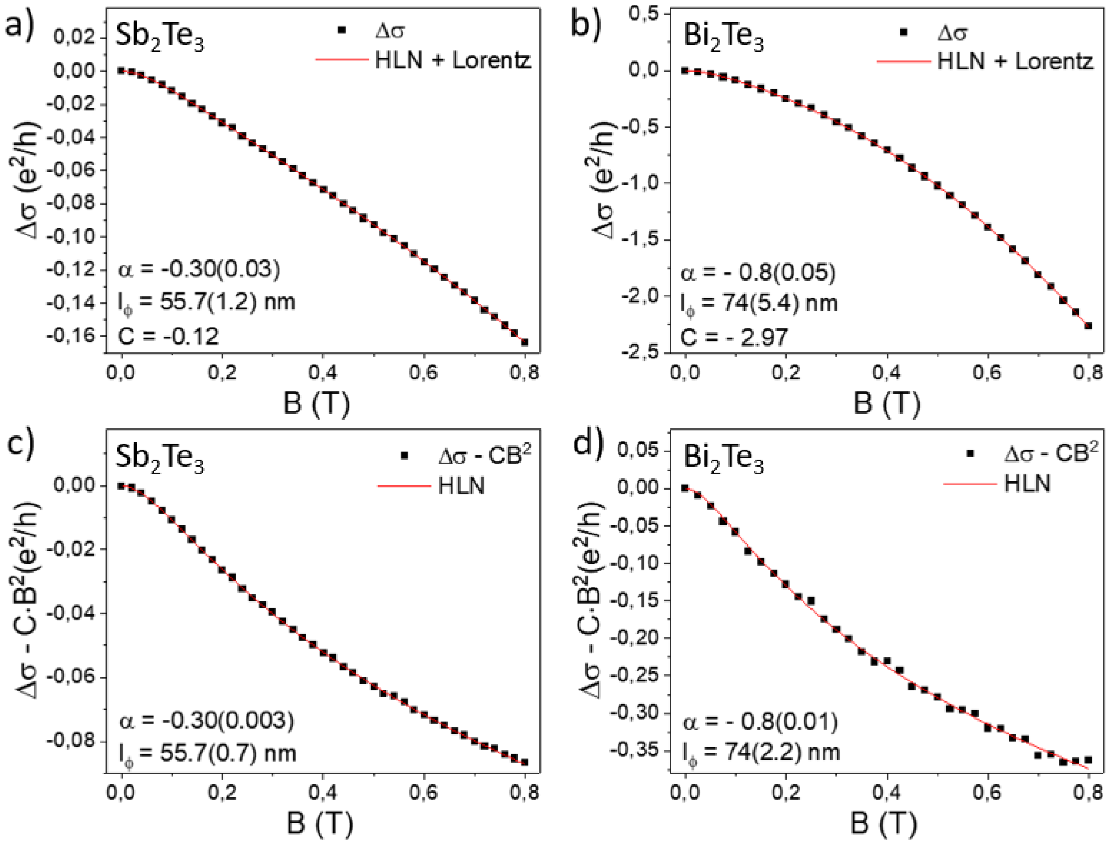

Figure 3.3: In panels (a) and (b), the MC curves measured at 5.5 K and fitted with the HLN equation comprehensive of the quadratic term (eq.2.6) are reported for Sb_2Te_3 and Bi_2Te_3 respectively. In panels (c) and (d) the MC signals are displayed, after removing the parabolic contribution to the fit, for Sb_2Te_3 and Bi_2Te_3 respectively. The HLN fit is performed again without the quadratic term using equation 2.5. Figure adapted from [81]

The $|\ \alpha\ |$ values extracted for the films of Sb_2Te_3 and Bi_2Te_3 are 0.3 and 0.8 respectively, suggesting that the the number of transport channels being governed by quantum diffusion is larger in Bi_2Te_3 than in Sb_2Te_3. Accordingly, l_ϕ = 74 nm in Bi_2Te_3 and l_ϕ = 55 nm in Sb_2Te_3, indicating that spin is, on average, conserved over o greater distance in Bi_2Te_3. On the other hand, the higher C parameter extracted for Bi_2Te_3 (~ -3) with respect to Sb_2Te_3 (~ -0.1) indicates that the BS play a more relevant role in the overall conduction mechanisms of Bi_2Te_3 than Sb_2Te_3 . Clearly, upon removing the quadratic term, the typical cusp-like MC is observed in Sb_2Te_3 (figure 3.1.2c)) and Bi_2Te_3 (figure 3.1.2d)), now quite well resembling the behaviour predicted by HLN theory as shown in figure 2.4 and the data reported in the literature for many TIs, in which the Fermi level is placed exactly in the middle of the BS band gap. [82, 23] The α and l_ϕ parameters extracted by subtracting the BS contribution (figure 3.1.2c,d)), are in perfect agreement with those obtained performing the HLN fit on the as-recorded MC data (figure 3.1.2a,b). In order to quantitatively compare Sb_2Te_3 and Bi_2Te_3 for what concerns their functionalities, the parameter γ is introduced, which is defined as the ratio between the MC without and with the inclusion of the CB^2 term (at the maximum magnetic field of 0.8T) as expressed in equation 3.1. For an ideal TI, with purely TSS-governed MC, we would expect $\gamma = 1$, while lower is the value toward zero, higher is the BS contribution in the overall transport mechanism.

$$\gamma = \frac{\Delta\sigma - C \cdot B^2[0.8T]}{\Delta\sigma[0.8T]} \tag{3.1}$$

The obtained γ is 0.16 for Bi_2Te_3 and 0.5 for Sb_2Te_3. This further supports that in Bi_2Te_3 the conduction from the BS is more relevant than in Sb_2Te_3 as it will be confirmed also by ARPES (see section 2.3.3). It is important to point out that the higher γ, obtained in Sb_2Te_3 than in Bi_2Te_3, is not in contrast with the higher α found in Bi_2Te_3 than in Sb_2Te_3, being the α value connected to the number of channels governed by quantum conduction, while the γ parameter gives an indication of the ratio between the number of the quantum conduction channels over the total transport channels.

Considering the HLN parameters extracted at 5-6 K for the MBE-grown Bi_2Te_3, [74, 83] the α and l_ϕ values obtained from our films turns out to be comparable. Differently, the α and l_ϕ values detected in Sb_2Te_3 are lower than those previously reported for Sb_2Te_3 films grown by MBE. [54] The different HLN parameters obtained for Sb_2Te_3 and Bi_2Te_3 can be interpreted in terms of their crystalline quality, being the latter ordered in a more epitaxial crystalline structure. In our publications [41, 42] the crystal structure of MOCVD-grown Sb_2Te_3 and Bi_2Te_3 was carefully investigated. The XRD pattern was collected in the Bragg-Brentano geometry, as shown in Figure 4 of Ref. [41] and in Figure 2 of Ref. [42], where, in both cases, the Full Width at Half Maximum (FWHM) of the [006] peak was measured along the rocking angle axis. In this experimental configuration, the evaluation of the FWHM provides information about the mosaicity of the crystal, which measures the broadening of the out-of-plane orientation of the crystalline grains of a film. For rhombohedral crystals such as Sb_2Te_3 and Bi_2Te_3, a lower mosaicity implies a better alignment of the c-axis (out-of-plane) of the crystals lattice. The two reported values, 0.46° for Sb_2Te_3 and 0.26° for Bi_2Te_3, suggest that the latter is composed by crystals with a lower dispersion around the c-axis. Being the crystals better aligned each other, macroscopically they generate a smother surface, which is in perfect agreement with the larger l_ϕ obtained in Bi_2Te_3 with respect to Sb_2Te_3.

As mentioned in section 2.1.1 Sb_2Te_3 was developed through several annealing steps with clear effect on the structural and morphological properties, showing the best crystalline quality for the films grown on an annealed substrate and $in-situ$ annealed after the growth. The results presented in the above section only concern the sample with the higher quality, however, the topological character was investigated also in the other films with different annealing steps. It was found that both the ”as-deposited” and the ”pre-annealed” samples (see section 2.1.1 for the definitions) shows a topological character, evidencing the existence of TSS with slightly lower quality than the one presented here. For a detailed report of the results obtained refer to the Appendix 1 or to [48].

3.1.3 WAL angular dependence

In order to decouple the WAL contribution purely arising from the 2D conduction of the TIs (i.e. their surfaces), from the 3D conduction from their “bulk” (i.e. BS), angular dependent-MC measurements have been conducted in all the MOCVD-developed TI, by following the methods introduced in section 2.3.2. In particular, to reveal the origin of the observed WAL, MC measurements are performed by applying the external magnetic field at different angles with respect to the samples’ plane. In the case of 2D-originated WAL, being intimately connected to 2D-topological states,, the MC characteristics must be solely proportional to the perpendicular component of the applied magnetic field. [57]

The thicknesses of the films are 30 nm and 90 nm for Sb_2Te_3 and Bi_2Te_3 respectively, due to this relatively high thickness the MC component arising from the BS is also expected to show up when the applied magnetic field is not necessarily perpendicular to the surface of the film. This is derived from the observation that the cyclotronic orbit, directly related to the existence of the Lorentzian force ($\propto \vec{v} \times \vec{B}$), is responsible for the deviation of part of the charge from their ordinary drift direction. Thus, inducing a BS-related MR effect observable also with a magnetic field applied parallel to the plane of the sample. [57]

Figure 3.4 reports the MC curves recorded with the field applied at different angles (θ) with respect to the plane of the samples and plotted as a function of the perpendicular component of the magnetic field ($B \cdot sin(\theta)$). In the adopted reference frame, $\theta = 0°$ is obtained when the field is applied in the plane of the sample and $\theta) = 90°$ when the field is completely perpendicular to the plane of the sample.

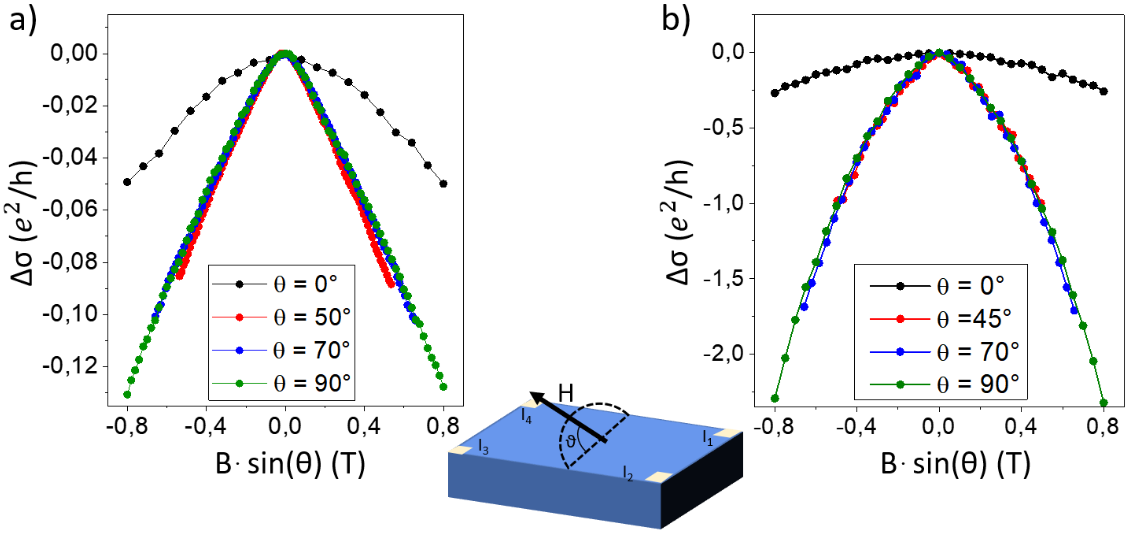

Figure 3.4: MC curves recorded at 5.5 K with the magnetic field applied at different angles with respect to the surface of Sb_2Te_3 in (a) and Bi_2Te_3 in (b). In both the panels the signal reported for $\theta = 0°$ is plotted as a function of the total in-plane field since in that configuration there is not a perpendicular component. Figure adapted from [81].

From Figure 3.4, it can be noticed that, even at $\theta = 0°$, a parabolic signal is still recorded, demonstrating that in such configuration it is exhibited a circular motion superimposed to the electronic drift driven by the applied voltage. This represents another indication that BS play a role in the transport mechanism of both the films and thus the magnetic Lorentzian force could induce a cyclotronic orbit even on planes not parallel to the surface of the TIs. On the other hand, being the presence of electrons in the TSS inherently 2D-confined (at the surfaces of the film), any field component at $\theta \neq 90°$, cannot excite any circular motion of carriers belonging to the TSS. In other words, the θ = 0° magnetic field component can only generate MC effects originating from the BS. The previous considerations indicate that the MC signals, which are proven to be directly proportional to the perpendicular component of the magnetic field, see figure 3.4, can be associated only to 2D conduction states. [57] For these reasons, the good overlapping between the signals, recorded over a wide range of angles of the magnetic field with respect the samples' surface and plotted as a function of the perpendicular component of the magnetic field (see figure 3.4), is a strong indication that the observed WAL originates from 2D conduction states in both the Sb_2Te_3 and Bi_2Te_3 TIs grown by MOCVD.

Following the typical interpretation for the value of α, in the case of Sb_2Te_3, its absolute value lower than 0.5 indicates that just one interface of the film exhibit Dirac-like band structure. Therefore, a possible interpretation for the obtained value of $|\alpha| = 0.3$ is that at 5.5 K, not all the existing quantum channels at the surface of the film are active. This, has not to be confused with the interpretation of the γ parameter which is related to the ratio between the conduction driven by TSS and the overall conduction mechanism, which could be different from 1 also in the case of ideal TSS but in the presence of a conducting bulk. On the other hands, for the Bi_2Te_3 films the obtained $|\alpha|$ value is very close to 1 and this could be associated with the presence of two interfaces showing conduction driven by 2D Dirac-like bands. Also in the case of Bi_2Te_3 we could attribute the fact that α is different from -1 due to a partial non activation of the TSS i.e. a slight non ideality of the TSS. According to the fact that the TSS are closer to ideality in Bi_2Te_3 than in Sb_2Te_3 the coherence length is slightly larger in Bi_2Te_3, meaning that here the electrons can conserve their spin state over a larger distance. This observation could be interpreted in terms of the surface quality of Sb_2Te_3 and Bi_2Te_3, being the latter slightly smoother (see section 2.1.1 and 2.1.2), it gives rise to higher quality TSS in Bi_2Te_3. Nevertheless, this is not in contrast with the lower γ of Bi_2Te_3 which gives an information about the high contribution of pure BS in the conduction mechanism.

3.1.4 Temperature dependence of the HLN parameters

In order to study on the evolution of the degree of intermixing between the TSS and BS the evolution of α and l_ϕ as a function of the temperatures is reported, as extracted from the HLN model using Equation 2.6.

In figure 3.5 the evolution of α and l_ϕ are reported in the 5 - 25 K temperature range. At higher temperature the parabolic contribution from the BS to the recorded MC becomes relevant, preventing us from making a reliable HLN analysis.

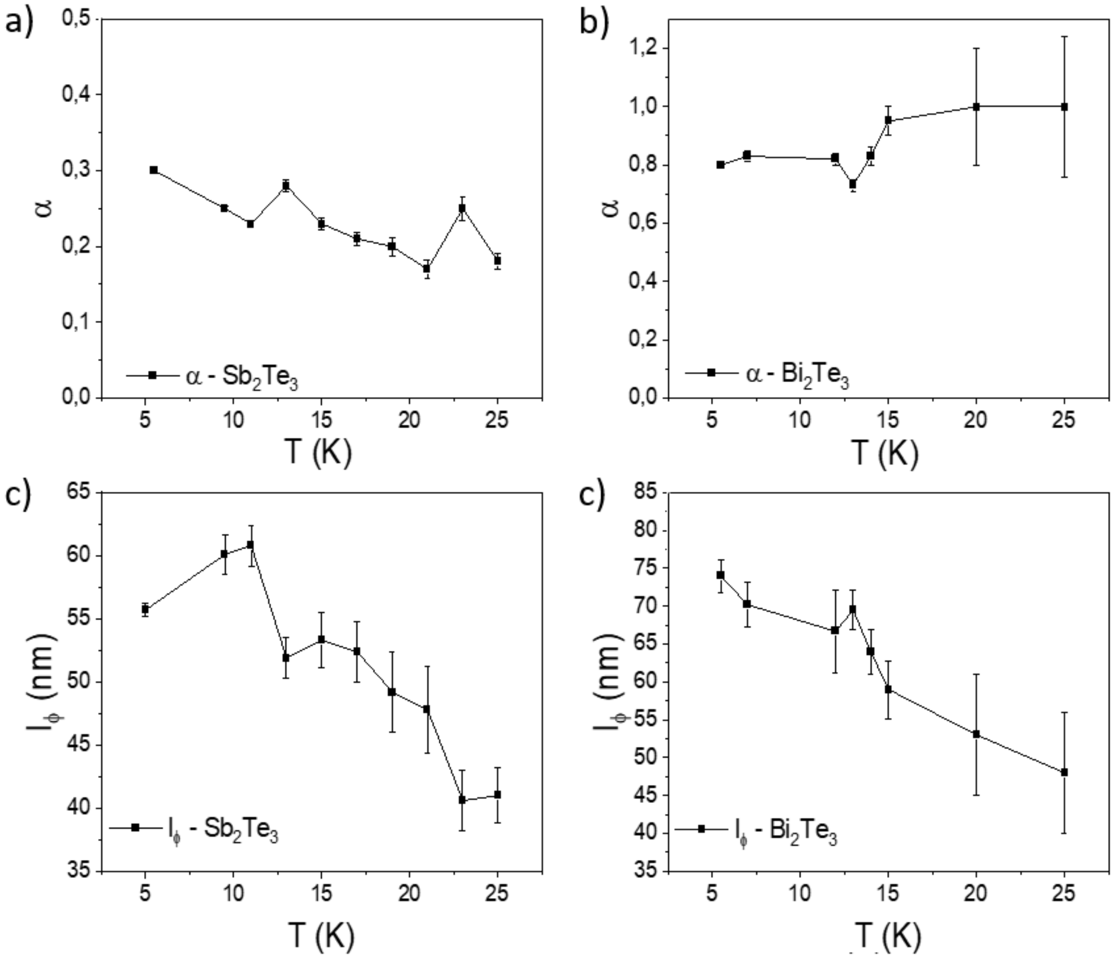

Figure 3.5: α and l_ϕ parameters as a function of the temperature in the 5 - 25 K range for Sb_2Te_3 in (a) and (c) and Sb_2Te_3 in (b) and (d) as extracted from equation 2.6.

In panel (a) of figure 3.5, it can be observed that the Sb_2Te_3 displays a slight reduction of the α parameter when the temperature increases from 5.5 to 25 K. This behaviour suggests that by increasing the temperature the BS affect more the electronic conduction, influencing the pure 2D Dirac-like transport in Sb_2Te_3. [79, 84] On the other hand, panel (b) of figure 3.5 shows how in the Bi_2Te_3 film α slightly increases until saturation in the 5-25 K temperature range, as also reported by others. [74] The evolution of l_ϕ as a function of the temperature is reported in panels (c) and (d) of figure 3.5 for Sb_2Te_3 and Bi_2Te_3 respectively. Here, a general decrease of l_ϕ is observed as a function of the increasing temperature for both the studied films, as expected. [73] In particular, for the ideal condition of completely independent TSS and BS, the l_ϕ should be proportional to T^{-p} with p = 0.5 as predicted by the Nyquist dephasing rate due to the 2D electron-electron interaction. [74, 79, 85, 86] In the presented case, to properly determine the p parameter was not possible, due to the bottom limit of the temperature range that we can explore. The obtained results indicate that the coupling between BS and TSS is quite stable as a function of the temperature in both the films. This stability is fundamental to predict that such TSS could, possibly, be detected also at room temperature, as it was recently confirmed by our work on spin-to-charge-conversion experiments performed at room temperature. [48, 71] The maximum temperature at which the WAL analysis was performed is determined by the increasing of the error bars affecting the data at temperature above 25 K, particularly in the case of Bi_2Te_3. An identification of the temperature at which the WAL effect disappears is not possible for the studied films, since both the TI present a MC signal composed by a clear sum of a quadratic contribution arising from the BS and a non-parabolic part due to the TSS.

3.1.5 Band structure imaging

The band structure is imaged by means of the ARPES system present at the NCSR 'Demokritos' in Athens, thus, before performing ARPES measurements, the film surface has to be properly cleaned as discussed in section 2.3.3. The contaminants present on the surface have been detected by means of XPS while the crystallographic quality of the surface is probed by means of RHEED.

Sample preparation

The samples were initially analyzed by RHEED to check that native oxide was present on the surface of the films. RHEED revealed no electronic reflection pattern that confirmed the presence of an amorphous layer on top of the crystalline film. To identify the elements composing the amorphous top layer XPS is performed (see section 2.5). After a first analysis it has been confirmed the massive presence of oxygen on the surfaces of both films (see black curve in 3.6 and 3.8). Indeed, an Ar^+ sputtering was performed to remove the oxide amorphous layer. The live-results obtained with the sputtering were recorded by means of the XPS measurement probing the variation of the concentration of Oxygen on the film surface. After several trials the optimal sputtering parameters were identified, for both Sb_2Te_3 and Bi_2Te_3, with an energy of 1.5 KeV and an Ar^+ pressure of 10^5 mbar for a duration of 255 s. In figure 3.6 an evolution of the XPS signal recorded in the film of Sb_2Te_3 is reported. It is clear that, on the unprocessed sample, the energies detected revealed the presence of the (expected) Sb-Te bond but also of the Sb-O and Te-O bonds which proved the existence of the oxide layer.

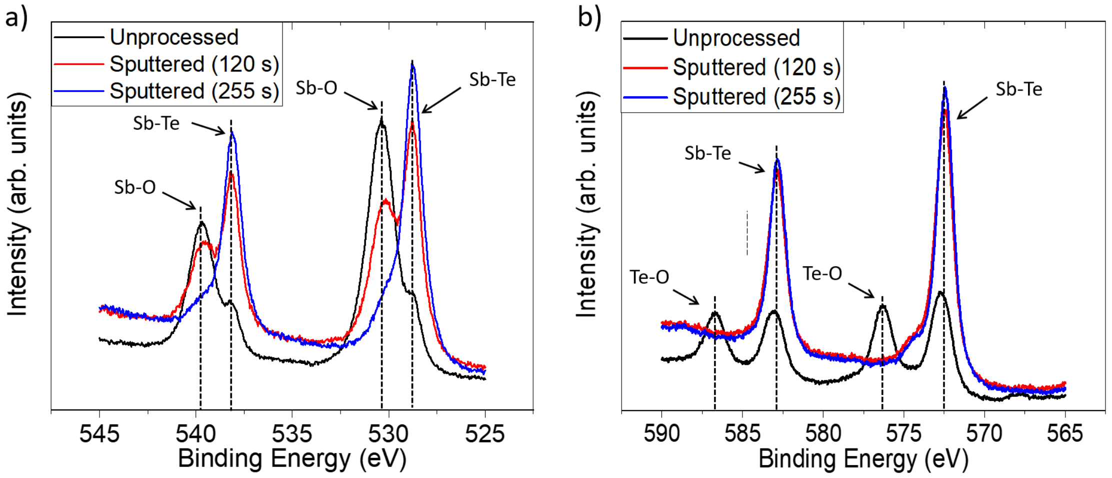

Figure 3.6: XPS spectra performed on the sample of Sb_2Te_3 after different duration of the Ar^+ sputtering. In panel (a) the energy of the 3d orbitals of Sb are shown, while panel (b) displays the 3d orbitals of Te.

In both panels (a) and (b) of figure 3.6 the black line represents the XPS signal detected from the unprocessed sample. It shows peaks that are shifted at lower energy with respect to the 3d orbitals of Sb and Te, thus, identifying the presence of Sb-O and Te-O bonds. After the first sputtering with a duration of 120 s, the peaks intensity corresponding to the Sb-O and Te-O bonds decreases while the intensity of the Sb-Te bonds is enhanced. After other 135 s of sputtering (255 in total) the XPS signal evidenced that the Sb-O and Te-O bonds were completely suppressed, thus the oxide layer was successfully removed.

After the sputtering the RHEED pattern was recorded to investigate the quality of the surface and an annealing at 292° C was performed to smooth and recover the surface. In figure 3.7 the pattern recorded after the various stages of the process to clean the surface are shown.

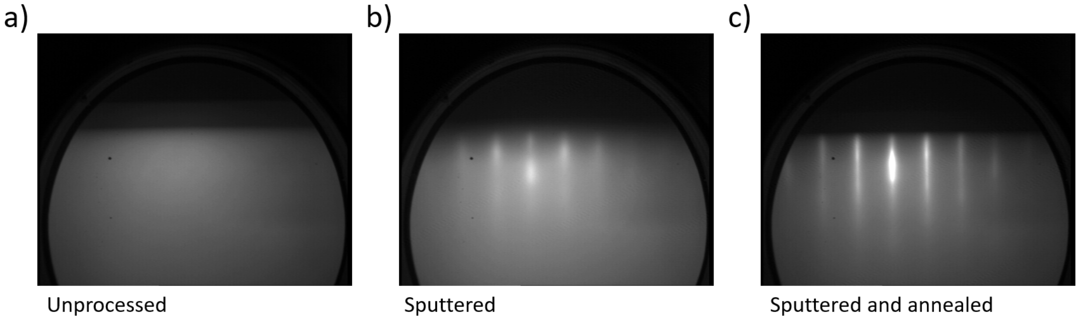

Figure 3.7: RHEED pattern for various stages of the process to clean the surface of the film: unprocessed in panel (a), sputtered (255 s) in panel (b) and sputtered (255 s) and annealed in panel (c).

It can be noticed that the unprocessed films, see figure 3.7a), did not produce any RHEED pattern due to the fact that the surface was completely oxidized and thus, amorphous. Differently, in figure 3.7b), a RHEED pattern was visible but not well defined, thus, the electrons had been diffracted from a crystalline surface but due to its poor quality the pattern was faded and not regular. Following a thermal annealing, see figure 3.7c), the RHEED pattern became clearly defined, thus demonstrating an almost full recover of the surface of Sb_2Te_3.

The same process was repeated for the film of Bi_2Te_3, and figure 3.8 shows the XPS spectra obtained to probe the bonding energy of the 4f orbitals of Bi and the 3d orbitals of Te. In this case the sputtering was carried on directly for 255 s.

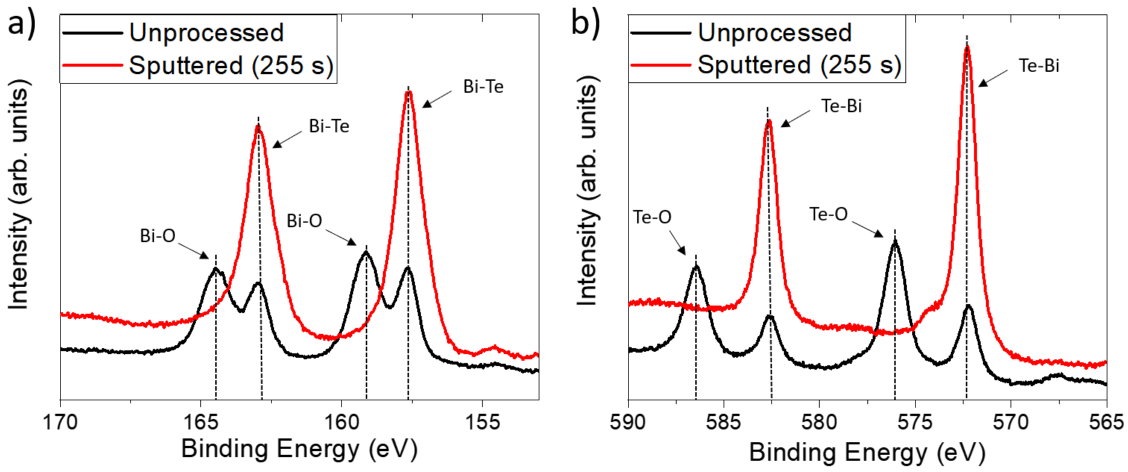

Figure 3.8: XPS spectra performed on the sample of Bi_2Te_3 after different duration of the Ar^+ sputtering. In panel (a) the energy of the 4f orbitals of Bi are shown, while panel (b) displays the 3d orbitals of Te.

The post-sputtering annealing is performed at 292° C as in the case of Sb_2Te_3 and the quality of the surface was probed again by means of RHEED. The RHEED pattern for Bi_2Te_3 is shown in figure 3.9 as taken at the various stage of the process.

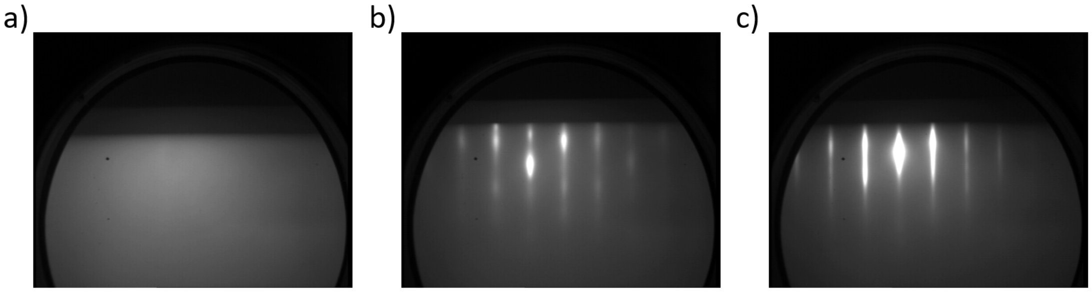

Figure 3.9: RHEED pattern for various stages of the process to clean the surface of the film: unprocessed in panel (a), sputtered in panel (b) and sputtered and annealed in panel (c).

ARPES spectra

After the TI surface treatment described in section 3.1.5 ARPES measurements were successfully conducted, and the results are shown in figure 3.10 with (a,c) and (b,d) respectively displaying the Sb_2Te_3 and Bi_2Te_3 band structure around the Γ point.

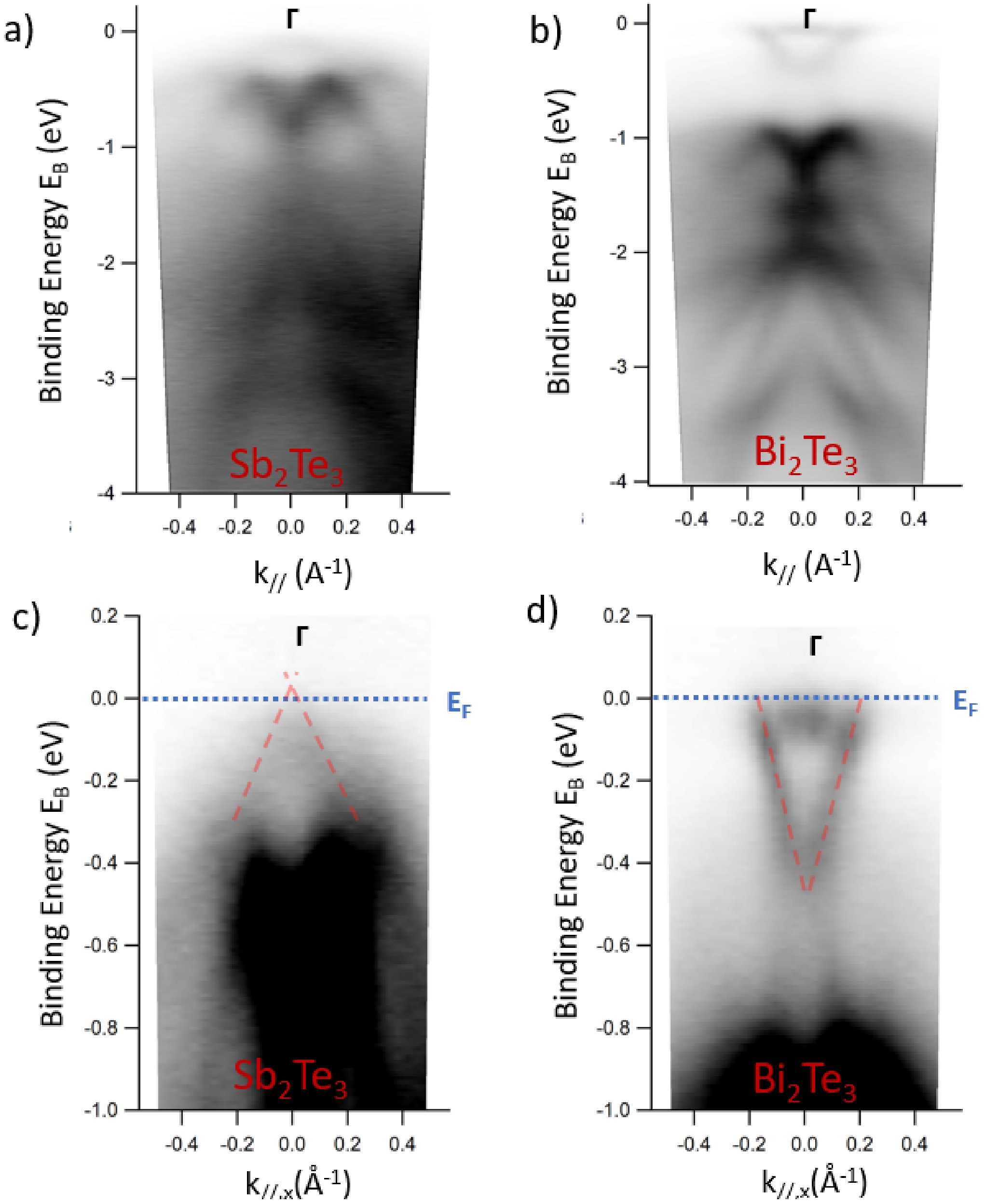

Figure 3.10: ARPES intensity maps obtained at room temperature for Sb_2Te_3 in (a,c) and for Bi_2Te_3 in (b,d). Panels (c) and (d) show a detail of the band structure close to the Fermi level covering energy values from 0.2 eV to -1 eV. The Fermi level is placed at zero energy and the connections between the valence and the conduction band, i.e., the TSS, are highlighted by the red dashed line. Picture adapted from [81].

In Figure 3.10(c,d), the surface states are highlighted with the red dashed lines. In the case of Sb_2Te_3 (panel (c)), the Dirac Point (DP), which is identified by the crossing point of the surface states, is very close to the Fermi level (~0.1 eV above it). Thus, approaching the ideal situation, in which the contribution of the TSS is dominant in the transport mechanism. This behaviour is also in agreement with the very marginal parabolic contribution observed in the corresponding MC curves (see figures 3.3). In the case of Bi_2Te_3, figure 3.10(b,d)), clearly evidences that the Fermi level crosses the conduction band at ~0.5 eV above the DP. This is very much in agreement with the (magneto)transport data as discussed in sections 3.3, where a relevant contribution from the BS to the overall conduction, has been identified. Considering that ARPES is a surface-sensitive technique, the observation of such a Dirac-like band structure, in both Sb_2Te_3 and Bi_2Te_3, is directly connected to the presence of TSS at the top surface of TIs.

As anticipated in section 3.1, from ARPES data we can directly measure the Fermi vector of the carriers, i.e. the intercept between the TSS (red dashed lines) and the Fermi level (blue dashed line). The two extracted values are $\sim 0.05\AA^{-1}$ for Sb_2Te_3 and $\sim 0.15\AA^{-1}$ for Bi_2Te_3. Then, by making use of equation 2.4, the carriers' MFPs can be calculated being, at 5.5 K, $\sim$ 4 nm in the case of Sb_2Te_3 and $\sim$ 70 nm for Bi_2Te_3. On the other hand, being the transport data taken at a wide range of temperature while ARPES is imaged at room temperature, the assumption of having a temperature-independent wave vector must be taken.

ARPES data are also recorded at constant energy, as a function of the in-plane wave vector ($\vec{k}_x$ and $\vec{k}_y$) to evaluate the symmetry of the band structure, as shown in figure 3.11(a,c) for Sb_2Te_3 and (b,d) for Bi_2Te_3. In figure 3.11 panels (a,b) show the results at the Fermi level, while panels (c,d) show the results at 0.2 eV and 0.15 eV below it for Sb_2Te_3 and Bi_2Te_3 respectively.

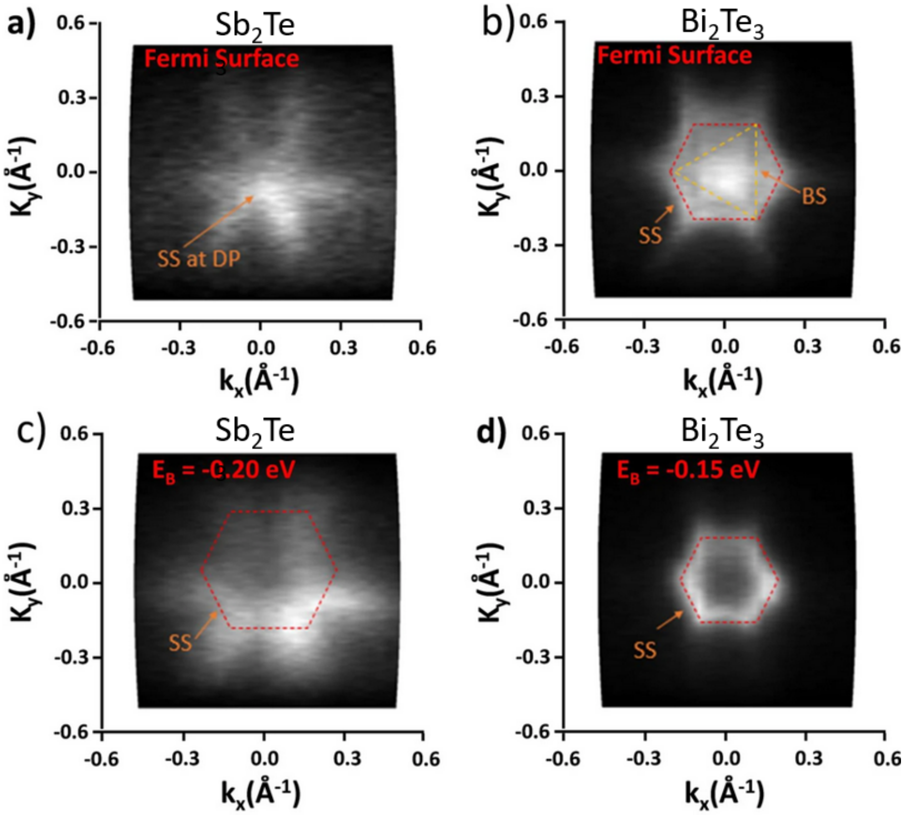

Figure 3.11: $\vec{k}_x$ and $\vec{k}_y$ constant energy contour plots obtained at different binding energies. In (a) and (b) it is shown the result for Sb_2Te_3 at the Fermi level and 0.2 eV below it respectively. In (c) and (d) it is shown the polar map of Bi_2Te_3 at the Fermi energy and 0.15 eV below it respectively.

It is clear from figure 3.11(a) for Sb_2Te_3, the ARPES signal, at the Fermi level, is characterized by an extremely bright point surrounded by an hexagonal faded pattern. Such a bright central point is interpreted as a clear signature of the DP, while the surrounding external hexagonal pattern is associated to the presence of the lower Dirac cone of the 2D-TSS, which is already partially occupied due to the thermal energy present at the room temperature. Such a picture is confirmed with the measure taken at 0.20 eV below the Fermi level, shown in figure 3.11(c), where the DP disappears while the hexagonal pattern remains evident, indicating that the TSS are still intercepted , but not yet the BS. Moreover, again in figure 3.11(c), it can be noticed that the apothem of the hexagonal TSS is larger than the apothem of the hexagon shown in (a), as expected while moving away from the DP along the Dirac cone.

The case of Bi_2Te_3 is different. At the Fermi energy we can clearly distinguish both a trigonal inner symmetry that is surrounded by a hexagonal external pattern, figure 3.11(b). The trigonal symmetry is attributed to the BS, which are clear and bright at the Fermi level further supporting the relevant bulk contribution to the electrical conduction. On the other hand, there is a clear superimposed hexagonal symmetry pattern, which identifies the existence of TSS at room temperature. The ARPES results are therefore in tight agreement with (magneto)transport data discussed in section 3.1.2. In particular, it is important to notice how, despite the strong BS contribution at the Fermi level, the TSS still can partially drive the conduction mechanism in the MOCVD-produced Bi_2Te_3. Recording ARPES at a decreased energy of 0.15 eV below the Fermi energy, figure 3.11(d), the trigonal symmetry is no more visible, indicating the disappearance of the BS at such energy. Otherwise that in the case of Sb_2Te_3, in Bi_2Te_3 the apothem of the hexagon is becoming smaller at 0.15 eV below the Fermi level, confirming that we are moving closer to the DP in this case, see figure 3.10(d) and 3.11(d).

The observation of the ARPES spectra allows also to make some considerations about the shape of the measured MC and the results emerged from the WAL analysis. As explained in section 3.3 the parameter γ, as defined in equation 3.1, is calculated for Sb_2Te_3 and Bi_2Te_3 and the results are: $\gamma = 0.5$ for Sb_2Te_3 and $\gamma = 0.16$ for Bi_2Te_3 . The parameter γ encodes information about the relative weight of the TSS in the transport mechanism indicating that in Sb_2Te_3 the TSS are more relevant than in Bi_2Te_3 in affecting the transport mechanism. This is in perfect agreement with the ARPES spectra shown in figure 3.10. The panel (c) confirms that in the case of Sb_2Te_3 the BS are not crossed by the Fermi level, thus, their poor contribution is due to the thermal energy that can activate some BS-related conduction channel. On the other hand, in the case of Bi_2Te_3, it is evident that the BS are relevant at the Fermi level, see figure 3.10(d) demonstrating that they are deeply involved in the conduction mechanism, which justifies the value of the γ parameter which is 4 times larger than the corresponding value in Sb_2Te_3.

Another meaningful observation could be done by considering the MFP at low temperature, as calculated above, being $\sim$ 4 nm for Sb_2Te_3 and $\sim$ 75 nm for Bi_2Te_3. As reported in Ref. [73] the WAL effect is more evident in materials where $l_\phi >> MFP$, being in accordance with the obtained MC results (see figure 3.3), where the WAL effect is quite clear for the Sb_2Te_3 while barely visible in the Bi_2Te_3 film. This result is also in perfect agreement with the higher $\gamma = 0.5$ observed in Sb_2Te_3, when compared with the $\gamma = 0.16$ obtained for Bi_2Te_3 where the Fermi level crosses the conduction band thus enhancing the BS contribution in the transport mechanism.

It is clear that, while the Sb_2Te_3 seems a mature TI in order to exploit functionalities connected to its TSS, still some work is needed to optimize the Bi_2Te_3 films. As a matter of fact, successful spin pumping into Sb_2Te_3 has been achieved in our group, [48, 71] and the promising results have been indeed attributed to the very clear TSS contribution at the Fermi level, as shown here by ARPES (this section) and MC data (section 3.1.2). On the other hand, despite the clear presence of BS at the Fermi level in Bi_2Te_3 the presence of the hexagonal symmetry attributed to the TSS motivated us to attempt spin pumping experiment as well. In the case of Bi_2Te_3, the results are indeed less clear and difficult to interpret, possibly due to the non-negligible involvement of BS in the conduction mechanism, as will be discussed in section 4. This, further motivated us to make efforts towards "purifying" the TSS from the BS contribution at the Fermi level in Bi_2Te_3 by attempting a Fermi level position-engineering through the development of Sb_2Te_3/Bi_2Te_3 heterostructures, as anticipated in section 2.1.3 and detailed, from a functional point of view, in section 3.2.1.

3.2 Heterostructure of $Si/Sb_2Te_3/Bi_2Te_3$

As anticipated in section 3.1.5 the optimization of the Fermi level position in Bi_2Te_3 is of fundamental importance to promote the conduction from TSS. As detailed in the sections 3.1.2 and 3.1.5 in Bi_2Te_3 it was found that the conduction mechanism relies on a combination of BS and TSS, thus making difficult to exploit the spin-momentum locking typical of the TSS. In this context, being motivated from several work in the literature [49, 50], we attempted a band structure engineering by growing a layer of Bi_2Te_3 (n-type carriers) on top of Sb_2Te_3 (p-type carriers). The growth details and the structural and morphological characterization are discussed in section 2.1.3 while, in the next section, it will be presented a characterization of the functionalities of the Sb_2Te_3/Bi_2Te_3 bilayer related to its topological character.

3.2.1 Magneto-electrical ordinary characterization and WAL analysis

After the ordinary structural and morphological characterization, discussed in section 2.1.3 the sample was characterized from an electric point of view, as shown in figure 3.12.

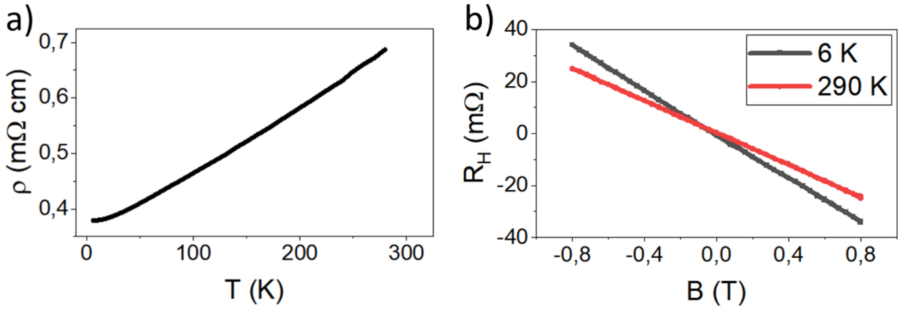

Figure 3.12: Resistivity in the 6 K - 290 K temperature range (a) and Hall resistance at 6 K and 290 K (b)

The resistivity, in the 6 K - 290 K temperature range, shows a metallic behavior (figure 3.12(a)) with a total decrease of 40 %, which, if compared with the 60 % decrease found in the single layer of Bi_2Te_3, indicates a lower metallic character. The Hall voltage has been recorded at 290 K and at 6 K showing, as expected, negative slope (figure 3.12b)), which is a clear signature of the electronic nature of the carriers. As detailed in section 2.2, from the Hall voltage measurements, is derived the carrier density, which is $1.7 \cdot 10^{-21} cm^{-3}$ at 290 K and $1.2 \cdot 10^{-21} cm^{-3}$ at 6 K, and the mobility, which is $5 cm^2 V^{-1} s^{-1}$ at 290 K and $14 cm^2 V^{-1} s^{-1}$ at 6 K. MC have been also measured at various temperatures and a comparison between the data obtained at 6 K (black line) and 290 K (red line) is shown in figure 3.13a).

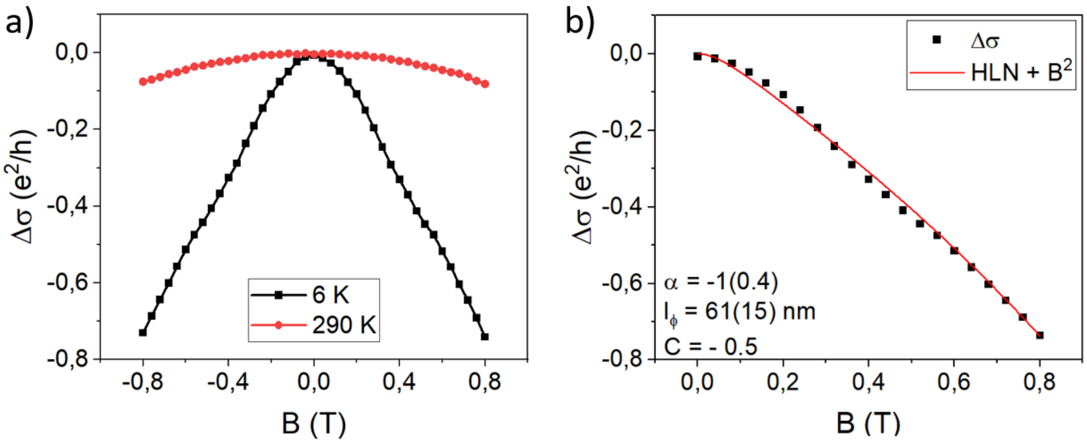

Figure 3.13: MC at 6 K (black) and 290 K (red) compared

In figure 3.13a) it can be noticed the difference between the MC signal recorded at 290 K and 6 K where the different shape is evident and the MC at 6 K shows clear cusp-like behavior. The signal at 6 K has been analyzed in the frame work of the HLN model, as explained in section 2.3.1, and the fit performed with equation 2.6 is shown in 3.13b). From the fit it is extracted an $\alpha = -1.0 \pm 0.2$ and a $l_\phi = 61 \pm 7nm$. These parameters are affected from errors that are more relevant than the ones obtained in Sb_2Te_3 and Bi_2Te_3 single layers and this effect could be attributed to the presence of a weak oscillation around 0.4 T, that is not predicted from the HLN model and thus introduces some errors in the fit. Following the typical interpretation of the parameter $\alpha = -1$ (see section 2.3.1) it indicates that both the top and bottom interfaces of the Bi_2Te_3 layer posses TSS and that they are close to be ideal. The l_ϕ = 61 nm is slightly shorter than what was found in the Bi_2Te_3 single layer and we could interpret this result by considering the greater roughness of the bilayer of Bi_2Te_3/Sb_2Te_3 with respect to the Bi_2Te_3 single layer, as discussed in section 2.1.3. The C parameter, related to the BS contribution to transport, is much lower than the one obtained in Bi_2Te_3 single layer (C $\sim$ -3) indicating that the BS are, just partially, committed in the conduction mechanism, thus suggesting that the Fermi level is no more crossing the bulk states, as will be discussed in section 3.2.2.

3.2.2 Band structure imaging

Sample preparation

After the electrical preliminary investigation reported in section 3.2.1 the band structure investigation was performed to directly visualize the TSS and verify the position of the Fermi level with respect to the DP. As it was done for the single layer, the ARPES spectra were recorded in the NCSR 'Demokritos' in Athens after the necessary surface treatment. Initially, the sample was loaded into the RHEED system to verify the surface conditions. As expected, RHEED revealed no electronics reflection pattern, thus indicating that a continuous oxide layer was capping the whole surface. XPS was then performed to identify the elements present on the surface of the film, as deduced from the bonding energy detected by the photoemission spectroscopy. In this case the relevant bonding are Bi-Te, Bi-O and Te-O that have been all detected at the expected energy (see figure 3.14). The sputtering was done with Ar^+ at 1.5 KeV and 10^5 mbar of pressure with a minimum sputtering duration settled to 150 s. In figure 3.14 it is shown the evolution of the XPS spectra on the unprocessed sample (black line), after the sputtering (red line) and after the final annealing (blue line). The final annealing, was done to recover and smoothing the surface from the sputtering, nevertheless, the annealing temperature has to be decreased from 292° C (used for Bi_2Te_3 single layer) to 270° C to avoid the peeling of the two layers of Sb_2Te_3 and Bi_2Te_3.

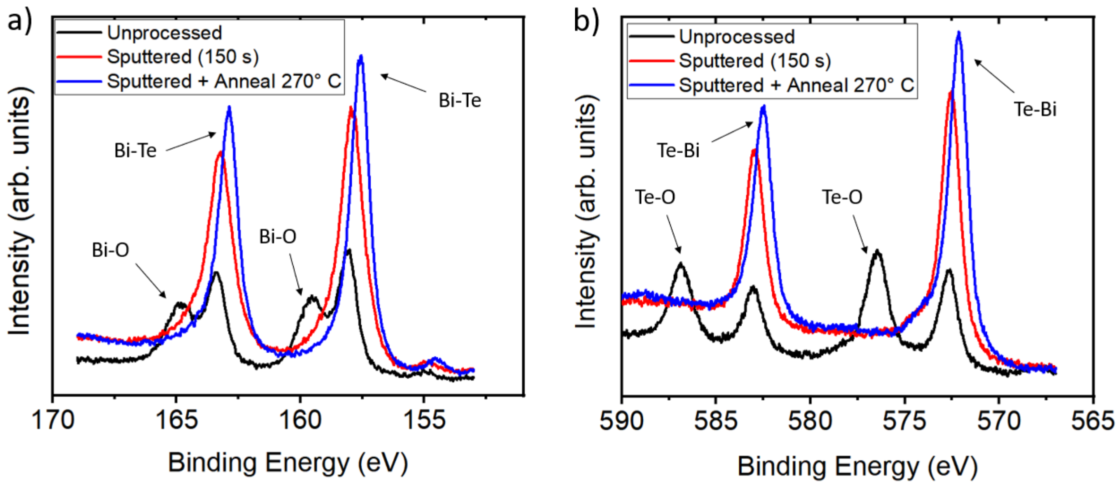

Figure 3.14: XPS spectra performed on the sample of Si/Bi_2Te_3/Sb_2Te_3 after 250 s of Ar^+ sputtering and after an annealing at 270 ° C. In panel (a) the energy of the 4f orbitals of Bi are shown, while panel (b) displays the 3d orbitals of Te.

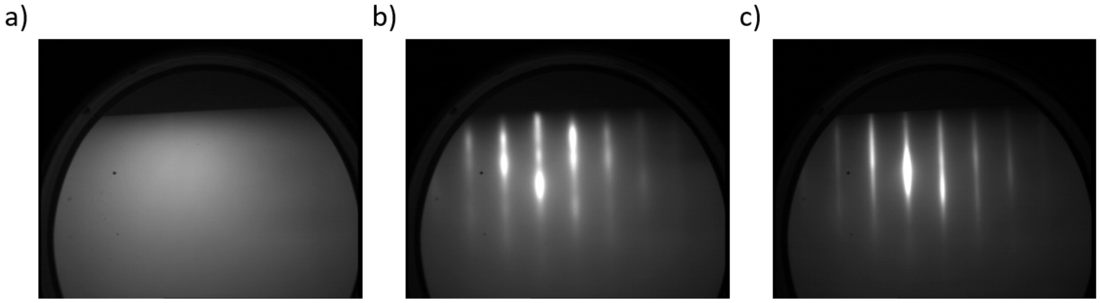

Figure 3.15: RHEED pattern for various stages of the process to clean the surface of the Si/Sb_2Te_3/Bi_2Te_3: unprocessed in panel (a), sputtered in panel (b) and sputtered and annealed in panel (c).

Moreover, to help the surface recovering and prevent the peeling of the two layers during the annealing it was introduced in the chamber a small amount of Te with the aim of replacing any Te atom if desorbed, since it is the most volatile element. By observing the XPS signal after the annealing in figure 3.14 (blue line) it can be seen that even the weak shoulder due to the Bi-O (panel (a)) and Te-O (panel (b)) bonds disappeared, thus the oxide layer was removed completely.

The RHEED pattern, shown in figure 3.15, was recorded on the unprocessed sample (panel a), after the sputtering of 150 s (panel b) and after the annealing (panel c).

It can be noticed that the unprocessed films 3.15a) does not produce any RHEED pattern due to the fact that the surface is completely oxidized and thus, amorphous. Figure 3.15b) shows a RHEED pattern visible but not well defined, indicating that the electrons have been diffracted from a crystalline surface but highly damaged. After a thermal annealing, in figure 3.15c) the RHEED pattern becomes clearly defined, thus demonstrating an almost full recover of the surface of the heterostructure.

ARPES spectra

After the successful cleaning of the surface from the oxide layer the ARPES measurement was performed at room temperature. The result has been compared with what was previously obtained for Bi_2Te_3 with specific focus in monitoring the Fermi level position with respect to the DP. Figure 3.16 displays a comparison of the band structure, around the Γ point of Bi_2Te_3 as a single layer (a) and Bi_2Te_3 grown on top of Sb_2Te_3 (b).

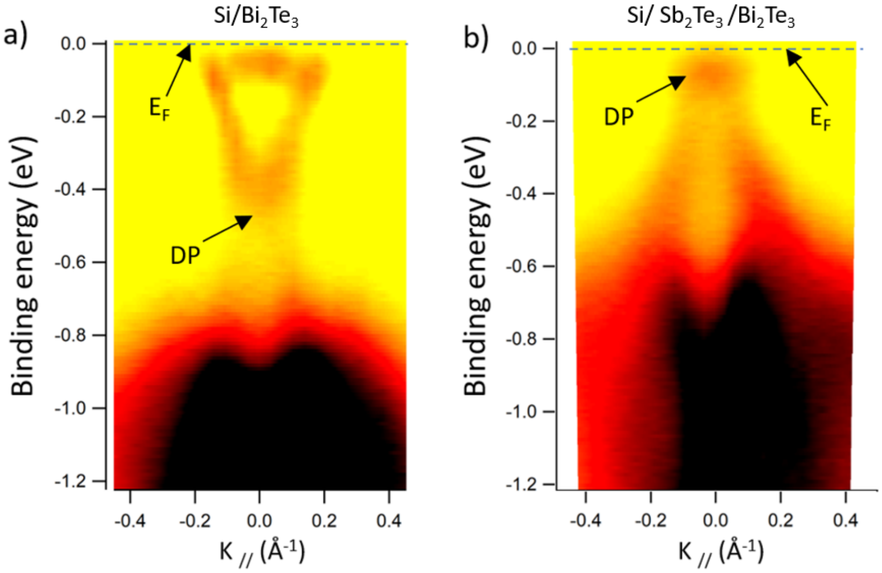

Figure 3.16: ARPES intensity map optained around the Γ point of Bi_2Te_3 (a) and Si/Sb_2Te_3/Bi_2Te_3 (b)

In figure 3.16(a,b) the Fermi level is placed at 0 eV and the binding energy explored are, in both cases, extended to -1.2 eV to make easier the comparison of the spectra. It is clear that in the Bi_2Te_3 grown on top of Sb_2Te_3 the Fermi level is shifted down towards the DP, not intercepting anymore the BS, suggesting that the seeds layer of Sb_2Te_3 influences the band structure of the top Bi_2Te_3 layer. As discussed later in the text. ARPES data are also collected at a constant energy, as a function of the in-plane wave vector ($\vec{k}_x$ and $\vec{k}_y$) to evaluate the symmetry of the band structure, as shown in figure 3.17(b,c,d,e).

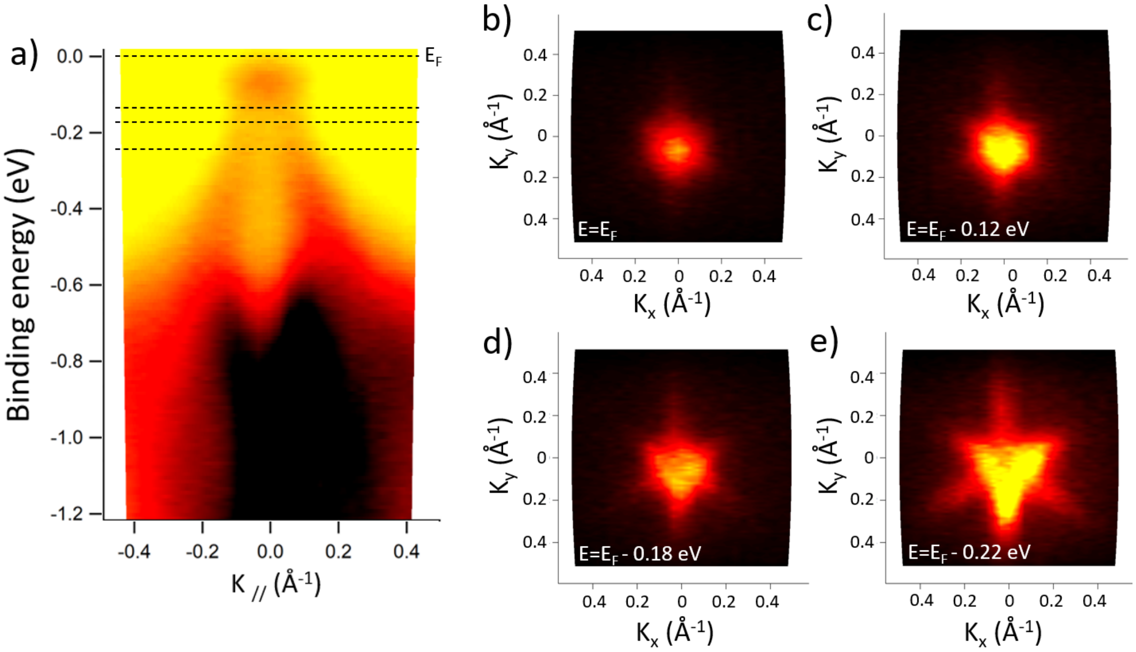

Figure 3.17: In panel (a) is shown the ARPES intensity map with dashed black line indicating the selected energy at which the constant energy contour plot has been recorded and shown in (b,c,d,e).

In figure 3.17b) the polar symmetry is associated to the extreme proximity to the DP, thus indicating that at the Fermi level the BS are not crossed. By decreasing the energy of -0.12 eV (figure 3.17c) an extremely bright point is still dominating the spectra, while a faded hexagonal pattern, associated to the TSS start to appear. By a further decrease of the energy of -0.18 eV below the Fermi level (figure 3.17d) an inner trigonal symmetry is observable, indicating that the BS come to play a role at this energy. Nevertheless an hexagonal pattern could be observed surrounding the bright inner trigonal spot, implying that at this energy also the TSS are still crossed at this energy. Figure 3.17e) displays the energy contour 0.22 eV below the Fermi level and a clear bright trigonal pattern is associated to the BS, while the surrounding hexagonal symmetry suggests that the TSS are still crossed even at this energy. The band structure analysis clearly indicates that the Fermi level is successfully shifted towards the band gap and the Fermi level position now corresponds to the DP position, thus justifying the minor parabolic signal observed in the MC and the α = -1 found following the HLN analysis.

For a thorough understanding of the phenomena at the basis of such a shift of the Fermi level towards the DP, further experiments are certainly needed. On the other hand, a tentative explanation could be discussed in the light of the results obtained from Pereira et. al. in [49]. In the experiment described in [49] several layers, with different thicknesses, of Sb_2Te_3 are grown on top of $\sim 6\,nm$ of Bi_2Te_3 and the ARPES recorded $in-situ$ is reported. They pointed out a different modification of the band structure of the material on top as a function of its thickness. Indeed, they observed a modification of the TSS shape while adding the first few layers of Sb_2Te_3 on top of Bi_2Te_3 while a rigid shift of the entire band structure (i.e. a chemical potential shift) when increasing the Sb_2Te_3 thickness up to $\sim 40\,nm$. In our case, by comparing the two panels of figure 3.16 a rigid shift of the Fermi energy (i.e. the chemical potential) is recognised, as could be noticed also from the unchanged distance between the DP and the BS. This observation is in good agreement with what was expected, following the results obtained in ref. [49] by assuming that similar mechanisms occurs also in reversed structure with Bi_2Te_3 on top of Sb_2Te_3. On the other hand, since Bi_2Te_3 is grown at 350 ° C we might expect also that, during its growth, a migration of Sb (which behave as a p-dopant) towards the Bi_2Te_3 layer took place, thus slightly compensating the n-doping of Bi_2Te_3 and contributing to the Fermi level shift observed also with a Bi_2Te_3 thickness $\sim 90\,nm$. In order to properly distinguish between the several phenomena that might contribute to the shifting of the Fermi energy in our sample further experiments are needed, starting from the growth of different thicknesses of the Bi_2Te_3 as top layer which is planned in the near future.

Due to the extreme proximity of the Fermi level and the DP it is tricky to precisely estimate the K_F in this situation, however we could safely define an upper limit being equal to 0.2 $\AA^{-1}$. Computing the MFP, by employing equation 2.4, with K_F = 0.2 $\AA^{-1}$ and μ = 14

$cm^2V^{-1}s^{-1}$, as obtained at 6 K (see section 3.2.1), it is obtained an upper limit for the MFP at 6 K of 2 nm. Being the l_ϕ = 61 nm, at the same temperature, this result indicates that $l_\phi >> MFP$ thus we can conclude that the spin coherence is conserved over several elastic scattering events, due to the topological nature of the conductive states. Again, this is in tight agreement with the fact that the shape of the MC for the sample of Sb_2Te_3/Bi_2Te_3 is not parabolic at all (see figure 3.13), differently with respect to what was discussed is section 3.1.5 for Bi_2Te_3 where it was found: $l_\phi \sim$ MFP.

Chapter 4

Exploring the TI functionalities in the TI/FM heterostructures

The demonstration of the existence of the TSS at the surface of the MOCVD-grown TIs opened the way for their integration into spintronics device. Following this demonstration we investigated the SCC by means of SP-FMR in the stack of TI/Au/Co/Au, as reported in section 4.1, and the magnetic response of a thin layer of 2D-FM, namely Cr_xTe_y alloy, on top of our MOCVD-grown TIs.

4.1 Spin pumping and FMR

Within this section, several experiments are described with the final aim to quantify the efficiency of the produced TIs as S2C converters. As detailed in section 2.4.1, to decouple the two possible origins of the SCC, namely the ISHE and the IEE, is not straightforward in material composed by heavy elements and where the TSS are present at the NM/FM interface. As discussed in section 3 among the three TIs investigated (Sb_2Te_3, Bi_2Te_3 and Sb_2Te_3/Bi_2Te_3) the one showing the most relevant contribution of the BS to the conduction mechanism is Bi_2Te_3, when grown on top of Si(111). Because of this reason, in such TI it would have been tricky to distinguish between ISHE or IEE originated SCC, thus we focused on the ”improved” version of it, i.e. the Bi_2Te_3 grown on top of Sb_2Te_3 where the conduction from BS was minimized (see section 3.13 and 3.16).

4.1.1 Sb_2Te_3

SP-FMR experiments were performed on Sb_2Te_3/Co-based heterostructures, with the aim of studying the charge current generated in the Sb_2Te_3 as a consequence of the spin current injected from the FM when brought in resonance conditions. By following a proper optimization of the chemical-structural and magnetic properties of the investigated systems, it was observed that the introduction of a Au interlayer of 5 (nm) was fundamental to protect the TSS of Sb_2Te_3 from the damage otherwise induced by the proximity of the Co layer, responsible of the time reversal symmetry breaking. [87]

In such a SP-FMR experiment a 3D spin current density is generated at resonance in the Co layers, longitudinally injected into the Sb_2Te_3 across the Au interlayer, and further electrically detected as a voltage drop at the edge of the Sb_2Te_3(/Au)/Co junction.

As discussed in the methods section (2.4.1), in a FMR experiment the presence of a TI underneath the FM could vary the total damping parameter (α) with respect the damping parameter obtained in the self-standing FM case (α_{ref}). The first goal of a SP-FMR experiment is therefore to determine the extra damping in the system due to the presence of the TI. As listed in table 4.1, different samples were fabricated in order to investigate the effect of the Sb_2Te_3 layer for an efficient SCC, as deeply discussed in Ref. [71]).

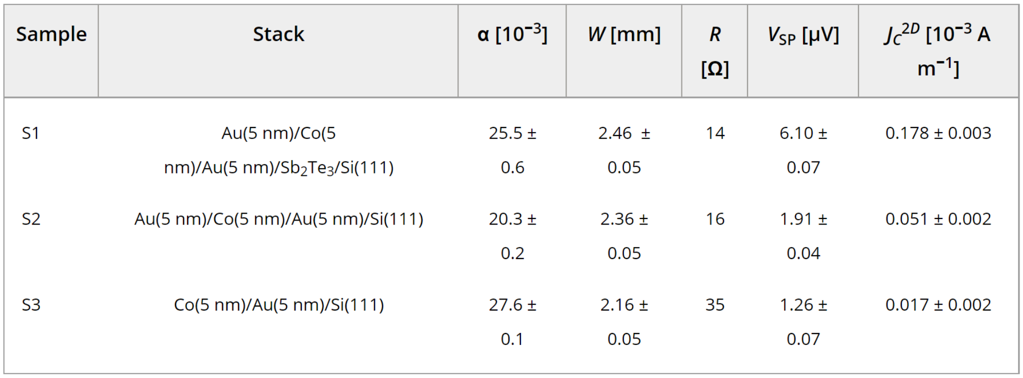

Sample	Stack	α [10^{-3}]	*W* [mm]	*R* [Ω]	V_{SP} [μV]	J_C^{2D} [10^{-3} A m^{-1}]
S1	Au(5 nm)/Co(5 nm)/Au(5 nm)/Sb_2Te_3/Si(111)	25.5 ± 0.6	2.46 ± 0.05	14	6.10 ± 0.07	0.178 ± 0.003
S2	Au(5 nm)/Co(5 nm)/Au(5 nm)/Si(111)	20.3 ± 0.2	2.36 ± 0.05	16	1.91 ± 0.04	0.051 ± 0.002
S3	Co(5 nm)/Au(5 nm)/Si(111)	27.6 ± 0.1	2.16 ± 0.05	35	1.26 ± 0.07	0.017 ± 0.002

Table 4.1: Summary of the main electrical and geometrical features of the investigates samples. The values of α and J_C^{2D} are calculated with a procedure that is detailed later in this section. Table from Ref. [71].

In table 4.1 the α and J_C^{2D} values are reported for the investigated samples, beside their sheet resistance R and width W.

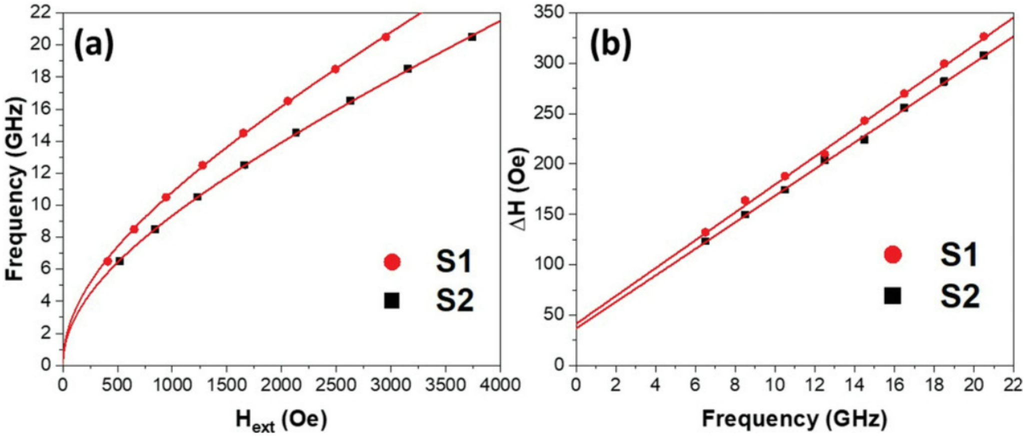

Figure 4.1: (a) Resonance frequency as a function of the resonance magnetic field for S1 and S2.(b) Signal linewidth as a function of the resonance frequency for the samples in panel (a). Figure from [71]

In figure 4.1(a) it is reported the resonance frequency of the FMR experiment as a function of the resonant magnetic field. By fitting the signals shown in figure 4.1(a) with the Kittel equation (2.10), the effective magnetization ($M_{eff} \sim M_s$) and the gyromagnetic ratio γ are extracted, as previously reported elsewhere [69, 70]. The latter quantities are used to calculate the total spin current density generated in a specific system. In Figure 4.1(b) the FMR signal linewidth is shown for samples S1 and S2 as a function of the resonance frequency. The data are fitted with equation 2.11 and the difference between the fitted slopes of the two lines (red solid lines) indicates the enhancement of the damping constant for the sample S1 containing the Sb$_2$Te$_3$ layer. By considering the extracted $\alpha_{S1} = (25.5 \pm 0.6) \cdot 10^{-3}$ and $\alpha_{S2} = (20.3 \pm 0.2) \cdot 10^{-3}$, a $g^{\uparrow\downarrow}_{eff,Sb_2Te_3} = 8.34 \cdot 10^{18} m^{-2}$ was derived by means of equation 4.1, which allows to calculate J_S^{3D} with equation 2.14.

$$Re(g^{\uparrow\downarrow}_{eff,Sb_2Te_3}) = \frac{4\pi M_s t_{FM}}{g\mu_B}(\alpha_{S1} - \alpha_{S2}) \tag{4.1}$$

The total spin current density associated to the presence of Sb$_2$Te$_3$ is $J_S^{3D} = 6.4 \cdot 10^5 Am^{-2}$. The electrically detected FMR (ED-FMR) was performed on samples S1 and S2 in order to estimate the SCC efficiency of the Sb$_2$Te$_3$-based system.

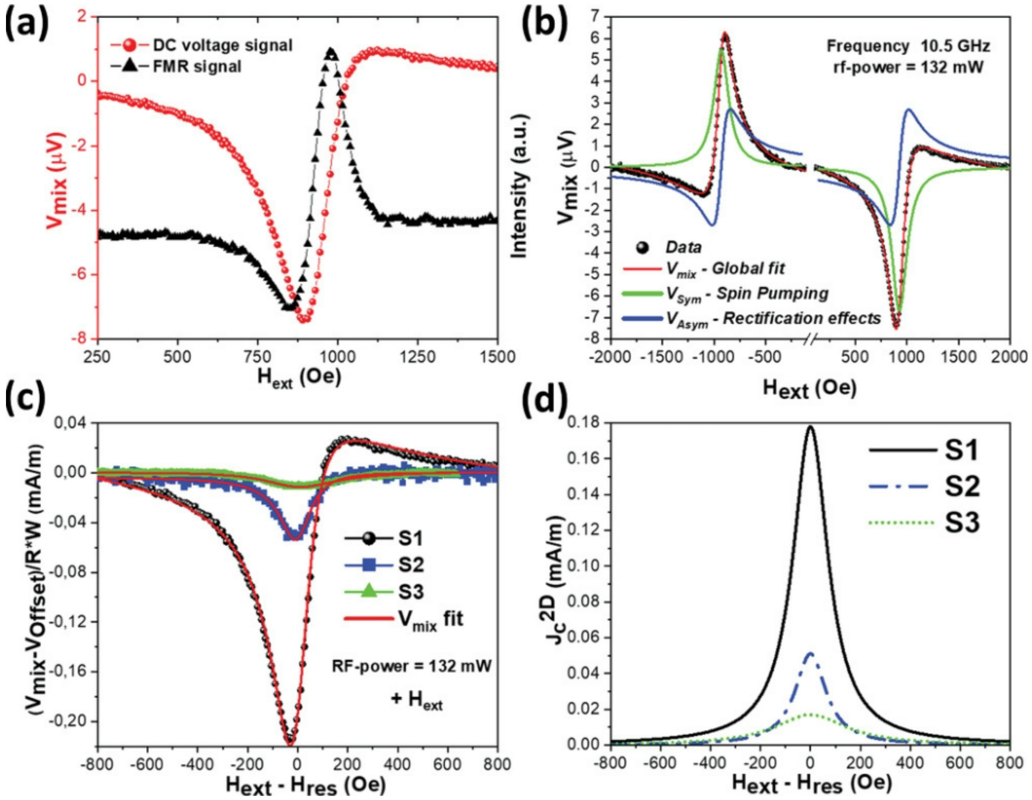

Figure 4.2: In (a) it is shown the SP DC voltage signal for sample S1 acquired at f = 10.5 GHz (red circles) and the FMR signal (black triangle). In (b) the total DC-voltage signal (black circles), the symmetric (green line) and antysymmetric (blue line) Lorentzian components are shown. The latter curves are plotted for both positive and negative magnetic field. In (c) the $V_{mix} - V_{offset}$ signals acquired for samples S1 (black dots), S2 (blue squares), and S3 (green triangles) and normalized over the R and W values are reported. In (d) the 2D charge current density extracted from the V_{sym} component of the V_{mix} signals reported in panel (a) and calculated using Equations 4.3 and 4.4 is shown. Figure from [71].

Figure 4.2(a) shows the DC voltage V_{mix} (known as mixing voltage) (red dot) and the FMR (black dot) signals acquired for S1 at a fixed resonance frequency. The two curves lie at the same resonant magnetic field, demonstrating that the electrical detection is connected to the FMR process. Such V_{mix} can be interpreted as the combination of a symmetric Lorentzian function V_{sym} and an antisymmetric one V_{asym}. Indeed, the V_{mix} signal can be fitted with equation 4.2, which allow the extraction of the V_{sym} and the V_{asym} components.

$$V_{mix} = V_{sym}\frac{\Delta H^2}{\Delta H^2 + (H - H_{res})^2} + V_{asym}\frac{\Delta H((H - H_{res}))}{\Delta H^2 + (H - H_{res})^2} \tag{4.2}$$

Where H and H_{res} are the applied and the resonant magnetic field, respectively, and ΔH is the FWHM signal linewidth. From the SP theory, [88, 89] the V_{sym} extracted from the fit in Equation 4.2 can be originated only from the SP contribution to the V_{mix} curve when acquired in the in-plain geometry configuration, thus ideally considered as V_{sym} = V_{SP}. However, it is important to notice that V_{sym} could also contain the thermal Seebeck effect,[61] and in order to extract the pure SP contribution, V_{SP} is typically obtained through equation 4.3.

$$V_{SP} = \frac{V_{sym}[+H_{ext}] - V_{sym}[-H_{ext}]}{2} \tag{4.3}$$

Differently, the V_{asym} term is originated from the anisotropic magnetoresistance and anomalous Hall effect in the Au/Co/Au trilayer, thus representing the so-called *spin rectification term*. The V_{mix}, V_{sym} and V_{asym} curves for sample S1 are shown in Figure 4.2(b) for positive and negative magnetic field. [89, 90, 91]

A comparison between the DC signals normalized over R and W measured for S1, S2 and S3 is shown in Figure 4.2(c). Here, the effect of the Sb_2Te_3 layer insertion is clearly evident, producing a significant increasing of the signal intensity. By fitting the V_{mix} signals extracted for each sample with equations 4.2 and 4.3, the V_{SP} is obtained and J_C^{2D} derived through the following relation

$$J_C^{2D} = \frac{V_{SP}}{WR} \tag{4.4}$$

The resulting J_C^{2D} for the three samples are shown in figure 4.2(d). As expected, in our measured J_C^{2D} there is a certain contribution from Au, as demonstrated also by the different J_C^{2D} detected in S2 and S3. Nevertheless, the presence of Sb_2Te_3 in sample S1 provides a gigantic extra contribution to the SCC, with a 250 % enhancement when compared to the reference S2 sample. Our main focus is now to translate the observed 250% increase in the SP contribution due to Sb_2Te_3 (Figure 4.2d)), into SCC efficiency. To undoubtedly separate the contribution to V_{SP} arising from bulk ISHE and interface IEE is not straightforward. On the other hand, in chapter 3 it has been shown the ARPES detection of TSS at the surface of Sb_2Te_3 at RT and it has been demonstrated that the topological effect detected arises mainly from the TSS. This, together with the fact that without the Au interlayer between Co and Sb_2Te_3 no SP effect was observed (see ref. [71]), strongly supports the SCC as intimately occurring through the TSS, thus being associated to the interfacial IEE. Following this interpretation, the SCC figure of merit is the λ_{IEE} which is calculated as $\lambda_{IEE} = J_C^{2D}/J_S^{3D} = 0.28\,nm$. This result is comparable or higher than what is usually obtained by employing MBE-grown TIs as spin-charge converter, [67, 92, 93, 94] thus, it constitute a "year zero" for the use of chemical methods to fabricate TIs for highly efficient S2C converters.

4.1.2 Sb_2Te_3/Bi_2Te_3

In this section, the SP-FMR preliminary studies performed on the Sb_2Te_3/Bi_2Te_3-based systems are discussed. The FMR measurements conducted on the Si/Au(5 nm)/Co(5 nm)/Au(5 nm) (S_{ref}) reference stack and on the Si/Sb_2Te_3/Bi_2Te_3/Au(5 nm)/Co(5 nm)/Au(5 nm) (S_{TI}) functional sample are reported in Figure 4.3. As detailed in section 4.1.1, the resonance frequency as a function of the resonant magnetic field is shown in figure 4.3(a) and fitted with the Kittel equation (2.10) to extract the M_{eff} and γ values. [69, 70]

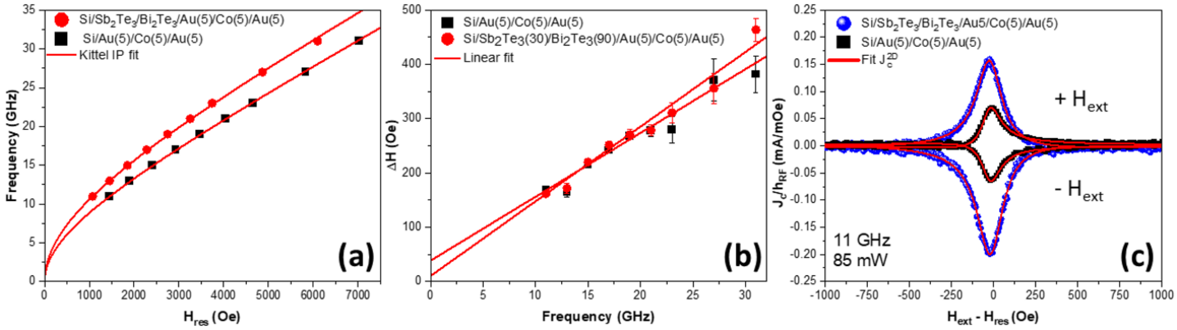

Figure 4.3: (a) Resonance frequency as a function of the resonance magnetic field for the for S_{ref} and S_{TI} samples. (b) Signal linewidth as a function of the RF frequency and (c) 2D charge current density converted in the TI layer for the samples in (a).

In figure 4.3(b) the linewidth broadening for various RF frequency is reported for S_{ref} and S_{TI}. As discussed in section 2.4.1, by linearly fitting such data with equation

2.11 it is possible to extract the value of α for S_{ref} and S_{TI} which in this case are equal to $\alpha_{S_{ref}} = (18.5 \pm 1.3) \cdot 10^{-3}$ and $\alpha_{S_{TI}} = (21.7 \pm 1.3) \cdot 10^{-3}$ respectively. Knowing the extra damping associated with the spin accumulation, we have $g^{\uparrow\downarrow}_{eff,TI} = 7.79 \cdot 10^{18} m^{-2}$ which, if inserted in equation 2.14, allows to calculate the pure spin current density $J_S^{3D} = 4 \cdot 10^5 Am^{-2}$. In order to calculate the SCC efficiency, also in this case the V_{mix} curve was extracted (Fig. 4.3(c))) and the spin pumping contribution derived. As a results a $\lambda_{IEE} = J_C^{2D}/J_S^{3D} = 0.32\,nm$ was calculated. Despite the obtained results are still preliminary, the SCC efficiency extracted for the Sb_2Te_3/Bi_2Te_3 bilayer turns out to be higher than the one calculate for the Sb_2Te_3 single layer, being compatible with the observed shift of the Fermi level towards the DP (3.16).

4.2 2D-magnetic layer of CrTe alloy deposited on top of the MOCVD-grown TIs

The integration of Van der Waals 2D-magnetic layer with topological materials is a very topical trend because of the potential application of a TI/2D-FM in the memory and logic field. A major issue when a 3D-FM is coupled with a TI is the very delicate interface between the two materials, moreover, it is well known that SCC or CSC are 2D effect, thus requiring extremely sharp and defined interfaces to host high quality TSS. Recently, Van der Waals 2D-FM have been proposed as potential thin films to improve the quality of the TI/FM interface, thus boosting the SCC or CSC efficiency in such a stack. One of the main advantage of this new materials resides in the fact that several TIs, among which Sb_2Te_3 and Bi_2Te_3 relies, as well, on Van der Waals bonds between their quintuple layers, thus, they may generate high quality and sharp interface. [95] Moreover, it has been demonstrated that several Van der Waals 2D-FMs could efficiently stabilize and host magnetic skyrmion, [96, 97] thus, a stack composed by TI/2D-FM could represent an ideal platform to stabilize and electrically control skyrmions.

Motivated by the recently published work of Figueiredo et. al. (see ref. [95]), investigating the high SOT found in MBE-grown Bi_2Te_3/CrTe2 we attempted the growth of CrTe-based alloy on top of our MOCVD-grown TIs.

Prior to the deposition of CrTe by MBE, the surface of the three TIs was cleaned and smoothed exploiting the same procedure thoroughly detailed in sections 3.1.5 and 3.2.2. As discussed in [95], CrTe could stabilize in different phases, indeed a precise control of the stoichiometry is complex due to the spontaneous possible Cr self-intercalation in the interlayer Van der Waals gaps. Depending on the substrate quality, deposition temperature and thickness of the film grown, several phases could be detected in the sample as $CrTe_2$, Cr_2Te_3, Cr_5Te_8 and Cr_3Te_4. Generally, it is not straightforward to grow single phase CrTe and is expected that, depending on the growth temperature and sample thickness, there will be a preponderant phase coexisting with the others. Our purpose is to obtain a 2D-FM with an accessible Curie temperature and perpendicular-to-plane magnetic anisotropy (PMA) to allow SOT investigation and, eventually, to look for the presence of stable skyrmions. These properties are usually associated with the Cr_2Te_3 and Cr_5Te_8 phases which are more-likely obtained with low growth temperature (250 °C - 300 °C) and in thin films ($t <\sim 15nm$). The growth details and the name associated to each sample are reported in table 4.2.

Sample	**Substrate**	**T_{growth} (°C)**	**Capping**
S1	Si (111) / Bi_2Te_3	300	~ 4 nm Al
S2	Si (111) / Sb_2Te_3	250	~ 4 nm Al
S3	Si (111) / Sb_2Te_3 / Bi_2Te_3	300	~ 4 nm Al

Table 4.2: Sample name and growth temperatures

After the growth, RHEED characterization was performed to reveal the surface crystalline arrangement and obtain an indication on the phases obtained. The results are shown in figure 4.4 which displays the electron streaky diffraction pattern for S1 (a,b), S2 (c,d) and S3 (e,f) showing a 2x2 reconstruction pattern and thus demonstrating that the preponderant phases are Cr_5Te_8 and Cr_3Te_4, [98] for all the films grown on top of the different TIs.

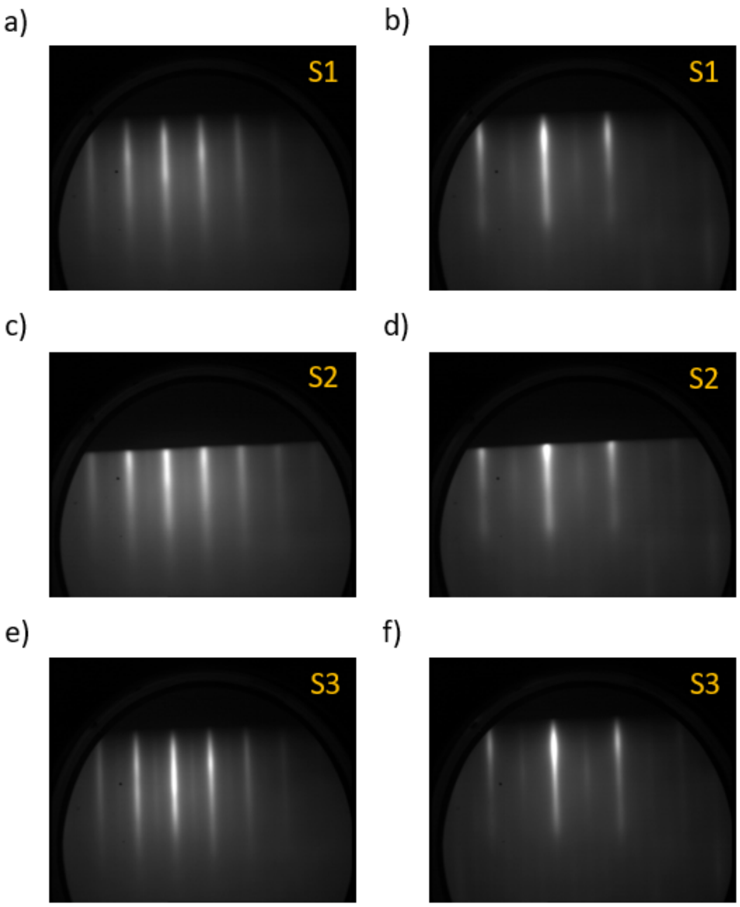

Figure 4.4: RHEED streaky reflection pattern along the two inequivalent direction $[1\bar{1}0]$ in (a,c,e) and $[11\bar{2}]$ in (b,d,f).

To protect the samples' surface they were capped with a 4 nm of Al which is then exposed to an Oxygen flux to oxidise the first layers as AlO_x.

The magnetic characterization was performed by means of temperature controlled MOKE microscopy with out-of-plane applied magnetic field to identify the Curie temperature and to reveal the magnetic loop at various temperature. Indeed, the coercive field necessary to switch the out-of-plane magnetization has been tracked as a function of the temperature, as shown in ref. 4.5.

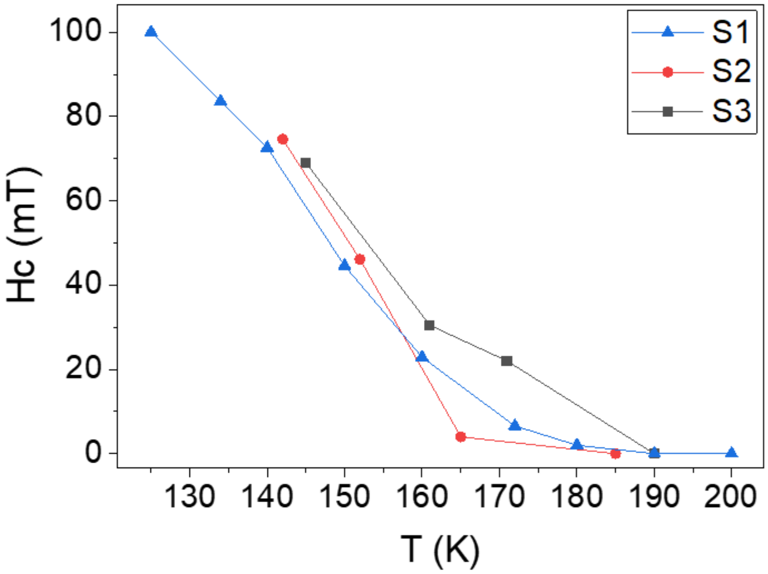

Figure 4.5: Coercive field at various temperature for S1, S2 and S3.

As it can be seen in figure 4.5, for all the three samples the Curie temperature is around 170 K and below 140 K it was not possible to saturate any of the samples, indicating that their coercive field is higher than 100 mT, which is the maximum magnetic field sustained from the available magnet. Focusing on the minimum temperature at which all the samples show a full switching of the magnetization, which is 140 K, the three loops are shown in figure 4.6.

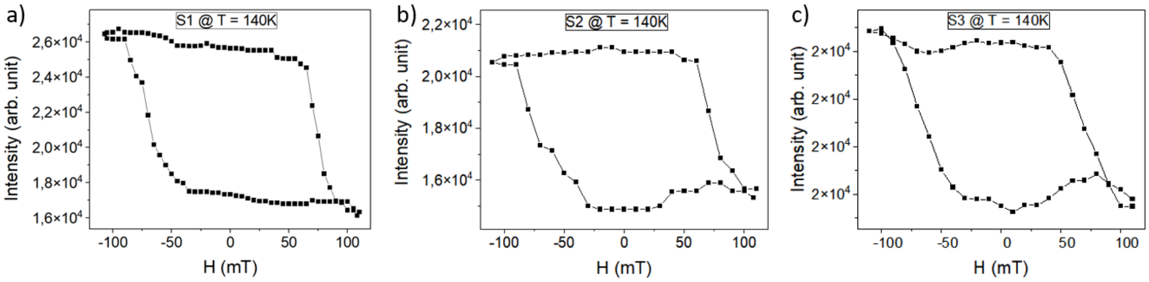

Figure 4.6: MOKE magnetic field loop performed at 140 K on the three samples as named in table 4.2.

These loops undoubtedly proved the existence of a PMA below the Curie temperature for all the three samples, thus confirming the successful MBE-growth of CrTe-based alloy on top of our MOCVD-grown TIs. Such magnetic properties are associated [98] with the

Cr_5Te_8 which is then assumed to be preponderant phase in our deposited films. Being the thickness of the CrTe layers $\sim 10\,nm$ for all the three samples, the observation of such a clean and well shaped magnetic loops indicates the existence of clean and sharp interfaces between the TIs and the 2D-FMs, paving the way for the investigation of SOT effect and skyrmions stabilization in such heterostructures which will be a topical issue in the next months.

Conclusions

Within this thesis are reported the main scientific results that I collected during my Ph.D., with the common thread of demonstrating the possibility of growing functional TIs by means of MOCVD technique on large-area Si substrates. To summarize, in sections 3.1.2 and 3.1.3 is discussed the magneto-electrical investigation of the topological character of Sb_2Te_3 and Bi_2Te_3. By means of the HLN model the MC was investigated extracting α, being proportional to the number of topologically conducting channel, and l_ϕ, which represents the average distance along which an electron could conserve its spin state. α and l_ϕ are extracted at 5.5 K resulting in an α equal to 0.3 and 0.8 for Sb_2Te_3 and Bi_2Te_3 respectively and a l_ϕ of 55 nm and 75 nm for Sb_2Te_3 and Bi_2Te_3 respectively. Moreover, by applying the external magnetic field at different angle, with respect to the film surface, it was possible to undoubtedly attribute the topological character observed to 2D states. From these measurements it was also observed that in Bi_2Te_3 even at 5.5 K the BS have a relevant role in driving the conduction mechanism, thus making such a material not ideal to isolate the topological effect and exploit it within devices. In section 3.1.5, with the aim of verifying that these 2D-Topological states are confined at the surface of the films, ARPES was employed and the clear Dirac-like band structure was imaged for both the materials, confirming the existence of high quality TSS in Sb_2Te_3 and Bi_2Te_3. ARPES also confirmed that in Bi_2Te_3 the Fermi level crosses the BS thus explaining the BS-related contribution to the global transport mechanism. Aiming to improve such a material from an electronic point of view, in section 3.2 with the purpose of limiting the BS contribution to transport in Bi_2Te_3, it was grown the stack composed by $Si/Sb_2Te_3/Bi_2Te_3$ with the goal of exploiting the different carriers type of the two TIs to shift the Fermi level position of Bi_2Te_3 towards the band gap (and the DP). The film obtained with this procedure was then characterized by means of MC analysis and fitted with the HLN equation which gave an ideal α = -1 and a l_ϕ = 61 nm, with a very marginal BS contribution observable in the MC. The ARPES spectra finally confirmed that the Fermi level was effectively, shifted, towards the band gap of the TI, minimizing the BS contribution to the global transport mechanism. In chapter 4 the focus is brought on the study of stacks composed by combination of TIs and FMs with the aim of opening the way for the realization of TIs-based device and the main results are listed below. The two films that revealed an almost ideal electronic band structure and transport mechanism closer to the one expected for ideal TI were Sb_2Te_3 and Sb_2Te_3/Bi_2Te_3. SP-FMR experiment were, indeed, carried out on stacks based on these films with the aim of estimating their potential as S2C converter materials (section 4.1). On top of both it was deposited the Au(5 nm)/Co(5 nm)/Au(5 nm) stack and by performing ED-FMR the SCC efficiency of a pure 3D spin current into a pure 2D charge current was quantified by means of the figure of merit λ_{IEE}. The two values obtained are $\lambda_{IEE} = 0.28\,nm$ and $\lambda_{IEE} = 0.32\,nm$ being comparable or higher with respect to the values usually obtained for MBE-grown TIs. This confirmed that MOCVD is an extremely promising method to grow TIs with industry compatible techniques representing a milestone in the integration of TIs within ordinary electronic. In section 4.2 it is reported the detailed deposition of the Van der Waals 2D-FM based on CrTe-based alloy. Recently these Van der Waals FM are attracting huge attention because of the extremely sharp and smooth interface which they form when coupled with chemically compatible TIs. We succeeded in growing the CrTe-based film with a thickness of 10 nm, on top of our MOCVD grown TIs and by means of MOKE microscopy it was revealed the PMA observed below 170 K (Curie temperature), thus suggesting the preponderance of the Cr_5Te_8 phase in such 2D-FM and confirming the existence of high quality TI/2D-FM interface.

List of scientific publication and participation to conference

1. Locatelli, L., Kumar, A., Tsipas, P., Dimoulas, A., Longo, E., Mantovan, R. (2022). Magnetotransport and ARPES studies of the topological insulators Sb_2Te_3 and Bi_2Te_3 grown by MOCVD on large-area Si substrates. Scientific Reports, 12(1), 3891.
2. Longo, E., Belli, M., Alia, M., Rimoldi, M., Cecchini, R., Longo, M., Wiemer C.

Locatelli L. ... Mantovan, R. (2022). Large Spin-to-Charge Conversion at Room Temperature in Extended Epitaxial Sb_2Te_3 Topological Insulator Chemically Grown on Silicon. Advanced Functional Materials, 32(4), 2109361.

3. Longo, E., Locatelli, L., Belli, M., Alia, M., Kumar, A., Longo, M., ... Mantovan, R. (2021). Spin-Charge Conversion in Fe/Au/Sb_2Te_3 Heterostructures as Probed By Spin Pumping Ferromagnetic Resonance. Advanced Materials Interfaces, 8(23), 2101244.

4. Kumar, A., Cecchini, R., Locatelli, L., Wiemer, C., Martella, C., Nasi, L., ... Longo, M. (2021). Large-area MOVPE growth of topological insulator Bi_2Te_3 epitaxial layers on i-Si (111). Crystal Growth Design, 21(7), 4023-4029.

List of Figures

Bibliography

[1] Robert R Schaller. “Moore’s law: past, present and future”. In: *IEEE spectrum* 34.6 (1997), pp. 52–59.

[2] Atsufumi Hirohata et al. “Review on spintronics: Principles and device applications”. In: *Journal of Magnetism and Magnetic Materials* 509 (2020), p. 166711.

[3] GA De Wijs and RA De Groot. “Towards 100% spin-polarized charge-injection: The half-metallic NiMnSb/CdS interface”. In: *Physical Review B* 64.2 (2001), p. 020402.

[4] C Leighton et al. “Composition controlled spin polarization in Co1- xFexS2 alloys”. In: *Journal of Physics: Condensed Matter* 19.31 (2007), p. 315219.

[5] A Fert and IA Campbell. “Two-current conduction in nickel”. In: *Physical Review Letters* 21.16 (1968), p. 1190.

[6] A Fert and IA Campbell. “Electrical resistivity of ferromagnetic nickel and iron based alloys”. In: *Journal of Physics F: Metal Physics* 6.5 (1976), p. 849.

[7] A Fert and IA Campbell. “Transport properties of ferromagnetic transition metals”. In: *Le Journal de Physique Colloques* 32.C1 (1971), pp. C1–46.

[8] Albert Fert. “Nobel Lecture: Origin, development, and future of spintronics”. In: *Reviews of modern physics* 80.4 (2008), p. 1517.

[9] Mario Norberto Baibich et al. “Giant magnetoresistance of (001) Fe/(001) Cr magnetic superlattices”. In: *Physical review letters* 61.21 (1988), p. 2472.

[10] Robert E Camley and J Barnaś. “Theory of giant magnetoresistance effects in magnetic layered structures with antiferromagnetic coupling”. In: *Physical review letters* 63.6 (1989), p. 664.

[11] Peter M Levy, Shufeng Zhang, and Albert Fert. “Electrical conductivity of magnetic multilayered structures”. In: *Physical review letters* 65.13 (1990), p. 1643.

[12] Terunobu Miyazaki and Nobuki Tezuka. “Giant magnetic tunneling effect in Fe/Al2O3/Fe junction”. In: *Journal of magnetism and magnetic materials* 139.3 (1995), pp. L231–L234.

[13] Jagadeesh Subbaiah Moodera et al. “Large magnetoresistance at room temperature in ferromagnetic thin film tunnel junctions”. In: *Physical review letters* 74.16 (1995), p. 3273.

[14] S Yuasa and DD Djayaprawira. “Giant tunnel magnetoresistance in magnetic tunnel junctions with a crystalline MgO (0 0 1) barrier”. In: *Journal of Physics D: Applied Physics* 40.21 (2007), R337.

[15] Sabpreet Bhatti et al. “Spintronics based random access memory: a review”. In: *Materials Today* 20.9 (2017), pp. 530–548.

[16] Kazutaka Yamane et al. “Spin torque switching of perpendicularly magnetized CoFeB-based tunnel junctions with high thermal tolerance”. In: *IEEE transactions on magnetics* 49.7 (2013), pp. 4335–4338.

[17] Stuart Parkin et al. “Magnetically engineered spintronic sensors and memory”. In: *Proceedings of the IEEE* 91.5 (2003), pp. 661–680.

[18] Chao Wang et al. “Advanced Spin Orbit Torque Magnetic Random Access Memory with Field-Free Switching Schemes”. In: *2020 IEEE 15th International Conference on Solid-State & Integrated Circuit Technology (ICSICT)*. IEEE. 2020, pp. 1–4.

[19] Shouzhong Peng et al. “Modulation of heavy metal/ferromagnetic metal interface for high-performance spintronic devices”. In: *Advanced Electronic Materials* 5.8 (2019), p. 1900134.

[20] Zongxia Guo et al. “Spintronics for energy-efficient computing: An overview and outlook”. In: *Proceedings of the IEEE* (2021).

[21] David Hsieh et al. “A topological Dirac insulator in a quantum spin Hall phase”. In: *Nature* 452.7190 (2008), pp. 970–974.

[22] David Hsieh et al. “Observation of unconventional quantum spin textures in topological insulators”. In: *Science* 323.5916 (2009), pp. 919–922.

[23] YL Chen et al. “Experimental realization of a three-dimensional topological insulator, Bi2Te3”. In: *science* 325.5937 (2009), pp. 178–181.

[24] Yuqi Xia et al. “Observation of a large-gap topological-insulator class with a single Dirac cone on the surface”. In: *Nature physics* 5.6 (2009), pp. 398–402.

[25] Haijun Zhang et al. “Topological insulators in Bi2Se3, Bi2Te3 and Sb2Te3 with a single Dirac cone on the surface”. In: *Nature physics* 5.6 (2009), pp. 438–442.

[26] Kushal Mazumder and Parasharam M Shirage. “A brief review of Bi2Se3 based topological insulator: From fundamentals to applications”. In: *Journal of Alloys and Compounds* 888 (2021), p. 161492.

[27] Reika Fujimura et al. “Current-induced magnetization switching at charge-transferred interface between topological insulator (Bi, Sb) 2Te3 and van der Waals ferromagnet Fe3GeTe2”. In: *Applied Physics Letters* 119.3 (2021), p. 032402.

[28] Jiahao Han et al. “Room-temperature spin-orbit torque switching induced by a topological insulator”. In: *Physical review letters* 119.7 (2017), p. 077702.

[29] Yi Wang et al. “Room temperature magnetization switching in topological insulator-ferromagnet heterostructures by spin-orbit torques”. In: *Nature communications* 8.1 (2017), pp. 1–6.

[30] Hao Wu et al. “Magnetic memory driven by topological insulators”. In: *Nature communications* 12.1 (2021), pp. 1–7.

[31] Can Onur Avci et al. “Current-induced switching in a magnetic insulator”. In: *Nature materials* 16.3 (2017), pp. 309–314.

[32] Luqiao Liu et al. “Spin-torque switching with the giant spin Hall effect of tantalum”. In: *Science* 336.6081 (2012), pp. 555–558.

[33] Ioan Mihai Miron et al. “Perpendicular switching of a single ferromagnetic layer induced by in-plane current injection”. In: *Nature* 476.7359 (2011), pp. 189–193.

[34] Albert Fert, Vincent Cros, and Joao Sampaio. “Skyrmions on the track”. In: *Nature nanotechnology* 8.3 (2013), pp. 152–156.

[35] Nikolai S Kiselev et al. “Chiral skyrmions in thin magnetic films: new objects for magnetic storage technologies?” In: *Journal of Physics D: Applied Physics* 44.39 (2011), p. 392001.

[36] Alexei N Bogdanov and DA Yablonskii. “Thermodynamically stable “vortices” in magnetically ordered crystals. The mixed state of magnets”. In: *Zh. Eksp. Teor. Fiz* 95.1 (1989), p. 178.

[37] A Bogdanov and A Hubert. “Thermodynamically stable magnetic vortex states in magnetic crystals”. In: *Journal of magnetism and magnetic materials* 138.3 (1994), pp. 255–269.

[38] Javier Osca and Bart Sorée. “Torque field and skyrmion motion by spin transfer torque in a quasi-2D interface in presence of strong spin–orbit interaction”. In: *Journal of Applied Physics* 130.13 (2021), p. 133903.

[39] Lee A Walsh et al. “Interface chemistry of contact metals and ferromagnets on the topological insulator Bi2Se3”. In: *The Journal of Physical Chemistry C* 121.42 (2017), pp. 23551–23563.

[40] Hao Wu et al. “Room-temperature spin-orbit torque from topological surface states”. In: *Physical review letters* 123.20 (2019), p. 207205.

[41] Martino Rimoldi et al. “Epitaxial and large area Sb 2 Te 3 thin films on silicon by MOCVD”. In: *RSC advances* 10.34 (2020), pp. 19936–19942.

[42] Arun Kumar et al. “Large-area MOVPE growth of topological insulator Bi2Te3 epitaxial layers on i-Si (111)”. In: *Crystal Growth & Design* 21.7 (2021), pp. 4023–4029.

[43] *aixtron web Kernel Description*. `https://www.aixtron.com/en/innovation/technologies/mocvd`.

[44] Jörn Kampmeier et al. “Selective area growth of Bi2Te3 and Sb2Te3 topological insulator thin films”. In: *Journal of crystal growth* 443 (2016), pp. 38–42.

[45] Frédéric Bonell et al. “Growth of twin-free and low-doped topological insulators on BaF2 (111)”. In: *Crystal Growth & Design* 17.9 (2017), pp. 4655–4660.

[46] Guang Wang et al. “Atomically smooth ultrathin films of topological insulator Sb2Te3”. In: *Nano Research* 3.12 (2010), pp. 874–880.

[47] Rabia Sultana et al. “Crystal growth and characterization of bulk Sb2Te3 topological insulator”. In: *Materials Research Express* 5.4 (2018), p. 046107.

[48] Emanuele Longo et al. “Spin-Charge Conversion in Fe/Au/Sb2Te3 Heterostructures as Probed By Spin Pumping Ferromagnetic Resonance”. In: *Advanced Materials Interfaces* 8.23 (2021), p. 2101244.

[49] VM Pereira et al. “Modulation of surface states in Sb 2 Te 3/Bi 2 Te 3 topological insulator heterostructures: The crucial role of the first adlayers”. In: *Physical Review Materials* 5.3 (2021), p. 034201.

[50] Takumi Sato et al. “Manipulation of Dirac cone in topological insulator/topological insulator heterostructure”. In: *ACS Applied Electronic Materials* 3.3 (2021), pp. 1080–1085.

[51] AA Ramadan, RD Gould, and A Ashour. “On the Van der Pauw method of resistivity measurements”. In: *Thin solid films* 239.2 (1994), pp. 272–275.

[52] Matthew Brahlek et al. “Transport properties of topological insulators: Band bending, bulk metal-to-insulator transition, and weak anti-localization”. In: *Solid State Communications* 215 (2015), pp. 54–62.

[53] Shinobu Hikami, Anatoly I Larkin, and Yosuke Nagaoka. “Spin-orbit interaction and magnetoresistance in the two dimensional random system”. In: *Progress of Theoretical Physics* 63.2 (1980), pp. 707–710.

[54] Y Takagaki et al. “Robust topological surface states in Sb 2 Te 3 layers as seen from the weak antilocalization effect”. In: *Physical Review B* 86.12 (2012), p. 125137.

[55] Sourabh Singh et al. “Linear magnetoresistance and surface to bulk coupling in topological insulator thin films”. In: *Journal of Physics: Condensed Matter* 29.50 (2017), p. 505601.

[56] G Bergmann. “Weak anti-localization—an experimental proof for the destructive interference of rotated spin 12”. In: *Solid State Communications* 42.11 (1982), pp. 815–817.

[57] K Shrestha et al. “Extremely large nonsaturating magnetoresistance and ultrahigh mobility due to topological surface states in the metallic Bi 2 Te 3 topological insulator”. In: *Physical Review B* 95.19 (2017), p. 195113.

[58] Cui-Zu Chang et al. “Band engineering of Dirac surface states in topological-insulator-based van der Waals heterostructures”. In: *Physical review letters* 115.13 (2015), p. 136801.

[59] Joseph Sklenar et al. “Perspective: Interface generation of spin-orbit torques”. In: *Journal of Applied Physics* 120.18 (2016), p. 180901.

[60] Ivan S Maksymov and Mikhail Kostylev. “Broadband stripline ferromagnetic resonance spectroscopy of ferromagnetic films, multilayers and nanostructures”. In: *Physica E: Low-dimensional Systems and Nanostructures* 69 (2015), pp. 253–293.

[61] Ken-ichi Uchida et al. “Observation of longitudinal spin-Seebeck effect in magnetic insulators”. In: *Applied Physics Letters* 97.17 (2010), p. 172505.

[62] J-C Rojas-Sánchez et al. “Spin to charge conversion at room temperature by spin pumping into a new type of topological insulator: α-Sn films”. In: *Physical review letters* 116.9 (2016), p. 096602.

[63] JC Sánchez et al. “Spin-to-charge conversion using Rashba coupling at the interface between non-magnetic materials”. In: *Nature communications* 4.1 (2013), pp. 1–7.

[64] Jairo Sinova et al. “Spin hall effects”. In: *Reviews of modern physics* 87.4 (2015), p. 1213.

[65] Victor M Edelstein. “Spin polarization of conduction electrons induced by electric current in two-dimensional asymmetric electron systems”. In: *Solid State Communications* 73.3 (1990), pp. 233–235.

[66] Mahdi Jamali et al. “Giant spin pumping and inverse spin Hall effect in the presence of surface and bulk spin- orbit coupling of topological insulator Bi2Se3”. In: *Nano letters* 15.10 (2015), pp. 7126–7132.

[67] Mahendra Dc et al. “Room-temperature spin-to-charge conversion in sputtered bismuth selenide thin films via spin pumping from yttrium iron garnet”. In: *Applied Physics Letters* 114.10 (2019), p. 102401.

[68] Yaroslav Tserkovnyak, Arne Brataas, and Gerrit EW Bauer. “Enhanced Gilbert damping in thin ferromagnetic films”. In: *Physical review letters* 88.11 (2002), p. 117601.

[69] A Ghosh et al. “Dependence of nonlocal Gilbert damping on the ferromagnetic layer type in ferromagnet/Cu/Pt heterostructures”. In: *Applied Physics Letters* 98.5 (2011), p. 052508.

[70] M Tokaç et al. “Interfacial structure dependent spin mixing conductance in cobalt thin films”. In: *Physical review letters* 115.5 (2015), p. 056601.

[71] Emanuele Longo et al. "Large Spin-to-Charge Conversion at Room Temperature in Extended Epitaxial Sb2Te3 Topological Insulator Chemically Grown on Silicon". In: *Advanced Functional Materials* 32.4 (2022), p. 2109361.

[72] John F Watts and John Wolstenholme. *An introduction to surface analysis by XPS and AES*. John Wiley & Sons, 2019.

[73] Rubén Gracia-Abad et al. "Omnipresence of weak antilocalization (WAL) in Bi2Se3 thin films: a review on its origin". In: *Nanomaterials* 11.5 (2021), p. 1077.

[74] Anupam Roy et al. "Two-dimensional weak anti-localization in Bi2Te3 thin film grown on Si (111)-(7× 7) surface by molecular beam epitaxy". In: *Applied Physics Letters* 102.16 (2013), p. 163118.

[75] Katharina Hoefer et al. "Intrinsic conduction through topological surface states of insulating Bi2Te3 epitaxial thin films". In: *Proceedings of the National Academy of Sciences* 111.42 (2014), pp. 14979–14984.

[76] SX Zhang et al. "Epitaxial thin films of topological insulator Bi2Te3 with two-dimensional weak anti-localization effect grown by pulsed laser deposition". In: *Thin Solid Films* 520.21 (2012), pp. 6459–6462.

[77] Nitesh Kumar et al. "Topological quantum materials from the viewpoint of chemistry". In: *Chemical Reviews* 121.5 (2020), pp. 2780–2815.

[78] Georg Bendt et al. "Deposition of topological insulator Sb 2 Te 3 films by an MOCVD process". In: *Journal of Materials Chemistry A* 2.22 (2014), pp. 8215–8222.

[79] Shao-Pin Chiu and Juhn-Jong Lin. "Weak antilocalization in topological insulator Bi 2 Te 3 microflakes". In: *Physical Review B* 87.3 (2013), p. 035122.

[80] James G Analytis et al. "Bulk Fermi surface coexistence with Dirac surface state in Bi 2 Se 3: A comparison of photoemission and Shubnikov–de Haas measurements". In: *Physical Review B* 81.20 (2010), p. 205407.

[81] L Locatelli et al. “Magnetotransport and ARPES studies of the topological insulators Sb2Te3 and Bi2Te3 grown by MOCVD on large-area Si substrates”. In: *Scientific reports* 12.1 (2022), pp. 1–10.

[82] Yuhung Liu et al. “Growth and characterization of MBE-grown (Bi1- xSbx) 2Se3 topological insulator”. In: *Japanese Journal of Applied Physics* 56.7 (2017), p. 070311.

[83] Hong-Tao He et al. “Impurity effect on weak antilocalization in the topological insulator Bi 2 Te 3”. In: *Physical review letters* 106.16 (2011), p. 166805.

[84] Hadar Steinberg et al. “Electrically tunable surface-to-bulk coherent coupling in topological insulator thin films”. In: *Physical Review B* 84.23 (2011), p. 233101.

[85] Boris L Altshuler, AG Aronov, and DE Khmelnitsky. “Effects of electron-electron collisions with small energy transfers on quantum localisation”. In: *Journal of Physics C: Solid State Physics* 15.36 (1982), p. 7367.

[86] L Plucinski et al. “Robust surface electronic properties of topological insulators: Bi 2 Te 3 films grown by molecular beam epitaxy”. In: *Applied physics letters* 98.22 (2011), p. 222503.

[87] AK Kaveev et al. “Energy-Gap Opening Near the Dirac Point after the Deposition of Cobalt on the (0001) Surface of the Topological Insulator BiSbTeSe 2”. In: *Semiconductors* 54 (2020), pp. 1051–1055.

[88] Yaroslav Tserkovnyak, Arne Brataas, and Gerrit EW Bauer. “Spin pumping and magnetization dynamics in metallic multilayers”. In: *Physical Review B* 66.22 (2002), p. 224403.

[89] O Mosendz et al. “Quantifying spin Hall angles from spin pumping: Experiments and theory”. In: *Physical review letters* 104.4 (2010), p. 046601.

[90] SM Rezende et al. “Enhanced spin pumping damping in yttrium iron garnet/Pt bilayers”. In: *Applied Physics Letters* 102.1 (2013), p. 012402.

[91] Wenxu Zhang et al. “Separating inverse spin Hall voltage and spin rectification voltage by inverting spin injection direction”. In: *Applied Physics Letters* 108.10 (2016), p. 102405.

[92] JBS Mendes et al. “Dirac-surface-state-dominated spin to charge current conversion in the topological insulator (Bi 0.22 Sb 0.78) 2 Te 3 films at room temperature”. In: *Physical Review B* 96.18 (2017), p. 180415.

[93] Praveen Deorani et al. “Observation of inverse spin Hall effect in bismuth selenide”. In: *Physical Review B* 90.9 (2014), p. 094403.

[94] Rui Sun et al. “Large Tunable spin-to-charge conversion induced by hybrid Rashba and Dirac surface states in topological insulator heterostructures”. In: *Nano Letters* 19.7 (2019), pp. 4420–4426.

[95] N Figueiredo-Prestes et al. “Large Fieldlike Spin-Orbit Torque and Magnetization Manipulation in a Fully Epitaxial van der Waals Two-Dimensional-Ferromagnet/Topological-Insulator Heterostructure Grown by Molecular-Beam Epitaxy”. In: *Physical Review Applied* 19.1 (2023), p. 014012.

[96] Yingying Wu et al. “Néel-type skyrmion in WTe2/Fe3GeTe2 van der Waals heterostructure”. In: *Nature communications* 11.1 (2020), p. 3860.

[97] Yingying Wu et al. “A van der Waals interface hosting two groups of magnetic skyrmions”. In: *Advanced Materials* 34.16 (2022), p. 2110583.

[98] Kinga Lasek et al. “Molecular beam epitaxy of transition metal (Ti-, V-, and Cr-) tellurides: From monolayer ditellurides to multilayer self-intercalation compounds”. In: *ACS nano* 14.7 (2020), pp. 8473–8484.